FABRICATION OF NANOSTRUCTURED SAMPLES FOR THE INVESTIGATION OF NEAR FIELD RADIATION TRANSFER

A THESIS SUBMITTED TO
THE GRADUATE SCHOOL OF NATURAL AND APPLIED SCIENCES
OF
MIDDLE EAST TECHNICAL UNIVERSITY

BY

ZAFER ARTVİN

IN PARTIAL FULFILLMENT OF THE REQUIREMENTS
FOR
THE DEGREE OF MASTER OF SCIENCE
IN
MICRO AND NANOTECHNOLOGY

AUGUST 2012

Approval of the thesis:

FABRICATION OF NANOSTRUCTURED SAMPLES FOR THE INVESTIGATION OF NEAR FIELD RADIATION TRANSFER

submitted by **ZAFER ARTVİN** in partial fulfillment of the requirements for the degree of **Master of Science in Micro and Nanotechnology Department, Middle East Technical University** by,

Prof. Dr. Canan Özgen ___________
Dean, Graduate School of **Natural and Applied Sciences**

Prof. Dr. Mürvet Volkan ___________
Head of Department, **Micro and Nanotechnology**

Assist. Prof. Dr. Tuba Okutucu ___________
Supervisor, **Mechanical Engineering Dept., METU**

Prof. Dr. M. Pınar Mengüç ___________
Co-Supervisor, **Mechanical Engineering Dept, Özyeğin University**

Examining Committee Members:

Prof. Dr. Raşit Turan ________________
Physics Department, METU

Assist. Prof. Dr. Tuba Okutucu ________________
Mechanical Engineering Dept., METU

Prof. Dr. M Pınar Mengüç ________________
Mechanical Engineering Dept, Özyeğin University

Assist Prof. Dr. Necmi Bıyıklı _________________
National Nanotechnology Research Center, Bilkent University

Inst. Dr. Özgür Bayer _________________
Mechanical Engineering Dept.,METU

Date: **28.08.2012**

Name, Last name **:** Zafer Artvin

Signature **:**

I hereby declare that all information in this document has been obtained and presented in accordance with academic rules and ethical conduct. I also declare that, as required by these rules and conduct, I have fully cited and referenced all material and results that are not original to this work.

To my wife Elif

and my son Bahadır…

ABSTRACT

FABRICATION OF NANOSTRUCTURED SAMPLES FOR THE INVESTIGATION OF NEAR FIELD RADIATION TRANSFER

Artvin, Zafer

M. Sc. Department of Micro and Nanotechnology

Supervisor: Assist. Prof. Dr. Tuba Okutucu

Co-Supervisor : Prof. Dr. M. Pınar Mengüç

August 2012, 72 pages

Radiative heat transfer in nanostructures with sub-wavelength dimensions can exceed that predicted by Planck's blackbody distribution. This increased effect is due to the tunneling of infrared radiation between nanogaps, and can allow the eventual development of nano-thermo-photo-voltaic (Nano-TPV) cells for energy generation from low temperature heat sources. Although near field radiation effects have been discussed for many years, experimental verification of these effects is very limited so far. In this study, silica coated silicon wafer sample chips have been manufactured by using MEMS fabrication methods for testing the near field radiation effects. A variety of samples with 1×1, 2×2 and 5×5 mm^2 area, and with 25 nm, 50 nm, 100 nm and 200 nm (nano-gap) separations have been prepared. 3D structures with vacuum gaps have been obtained by bonding of the silica coated wafers. The samples have been tested in an experimental setup by a collaborative group at Özyegin University, İstanbul. An increase in the net radiation heat transfer with decreasing nano-gap size has been reported by the Özyeğin group who used these samples in a parallel study. The thesis outlines the micro-fabrication techniques used for the sample preparation. Also, the manufacturing problems we have faced during this research program are discussed.

Keywords: Near field radiation, thermo-photo-voltaics, micro-fabrication, nano-gap, radiation tunneling, wafer bonding.

ÖZ

YAKIN ALAN IŞINIM AKTARIMINI İNCELEME AMACIYLA NANO-YAPI ÖRNEKLERİNİN ÜRETİMİ

Artvin, Zafer

M. Sc. Department of Micro and Nanotechnology

Tez Yöneticisi: Yrd. Doç. Dr. Tuba Okutucu

Ortak Tez Yöneticisi : Prof. Dr. M. Pınar Mengüç

Ağustos 2012, 72 sayfa

Dalgaboyundan küçük boyutlara sahip nano-yapılarda ışınım ile ısı aktarımı, Planck kara cisim dağılımı ile tahmin edilenden daha fazla olabilmektedir. Bu artış, kızılötesi ışınımın nanometre boyutundaki boşluklardan tünellemesi nedeniyle ortaya çıkmakta, ve düşük sıcaklıktaki ısı kaynaklarından elektrik enerjisi üretimi için nano-termo-fotovoltaik (Nano-TPV) hücrelerin geliştirilmesine olanak sağlamaktadır. Yakın alan ışınım etkileri uzun süredir tartışılmakla beraber, bu etkilerin doğrulanmasına yönelik deneysel çalışmalar halen oldukça sınırlıdır. Bu çalışmada, yakın alan ışınım etkilerinin test edilmesi amacıyla, silika kaplı silisyum pul örnekleri, MEMS üretim teknikleri kullanılarak üretilmiştir. 1×1, 2×2 ve 5×5 mm^2 alan, ve 25 nm, 50 nm, 100 nm ve 200 nm boşluğa sahip çeşitli örnekler hazırlanmıştır. Silika kaplı pulların birleştirilmesi ile üç boyutlu nanoboşluklu yapılar elde edilmiştir. Üretilen örnekler, Özyeğin Üniversitesi'nde yer alan bir ortak çalışma grubu tarafından, bir deney düzeneğinde test edilmiştir. Nano-boşluk boyutundaki azalmanın net ışınım ısı aktarımında artış sağladığı, örnekleri paralel bir çalışmada kullanan Özyeğin grubu tarafından raporlanmıştır. Bu araştırma çalışmasında ağırlıkla, örnek hazırlamada kullanılan mikro-üretim teknikleri üzerinde durulmuştur. Üretim sırasında karşılaşılan zorluklar da tartışılmıştır.

Anahtar kelimeler: Yakın alan ışınımı, termo-foto-voltaik, mikro-üretim, nano-boşluk, ışınım tünelleme, pul birleştirme.

ACKNOWLEDGEMENTS

I wish to thank my supervisor Assist. Prof. Dr. Tuba Okutucu who helped me supported me in every stage of my thesis and to my co-supervisor Prof.Dr. M. Pınar Mengüç.

The author also would like to thank to David Kurt Webb who worked hard for designing , establishing test setup and performing measurements.

I also want to thank to Dr. Necmi Bıyıklı and Mustafa Kemal Ruhi at UNAM Bilkent University and Prof. Dr. Hayrettin Yücel principal of METU-CENTRAL Laboratories where fabrication and characterization partially took place. I would like to thank to Prof.Dr. Raşit Turan who provided thermal oxidation furnace and wire cutter at GUNAM Labs.

I would like to thank G. Mittendorfer and M.Pawlak who managed and performed wafer bonding process at EV Group Laboratories in Austria. The author would also like to thank Dr. İbrahim Çam for his suggestions and comments.

This project supported by TUBİTAK Grant No: 109M170.

TABLE OF CONTENTS

ABSTRACT…………………………………………………………………….. vi
ÖZ……………………………………………………………………………. vii
ACKOWLEDGEMENTS……………………………………………………. viii
LIST OF TABLES……………………………………………………………… xi
LIST OF FIGURES…………………………………………………………… xii
LIST OF SYMBOLS/ABBREVATIONS……………………………………. xiv
CHAPTER
1. INTRODUCTION.. 1
1.1 Motivation ....…………………………………………... 1
1.2 Literature Review……………………………………………………. 7
1.3 Objective of this Thesis……………………………………………..... 15
2. SAMPLE DESIGN.. 18
2.1 Materials 18
2.1.1 Silicon Wafer.. 18
2.2.1 SiO_2…………………………..……………………….………………… 19
2.2. Sample Design ……………………..………………………………….……… 20
2.3 Design Calculations... 23
2.3.1 Deflection…………………………………………………………………….. 23
2.3.2 Vacuum Lifetime……………………..……………..……………………... 25
2.3.3 Conduction Heat Transfer Through Air Inside the Gap................................. 28
3. SAMPLE FABRICATION... 31
3.1Fabrication Steps……………..…………………….. 31

3.1.1 Oxidation of Silicon Wafer.........…………………...……………………….. 33

3.1.2 Lithography……………………………………………………………... 38

3.1.3 Wafer Bonding………………………………………………………….. 43

3.1.4 Wafer Dicing……………………………………………………………. 47

3.2 Discussion on Fabricated Samples……………………………………………... 48

3.3 Test Setup …………………………....…………………………………… 51

3.4 Preliminary Test results……………………………...……………………… 53

4. DICUSSIONS and CONCLUSIONS... 56

4.1 Discussion and Conclusions…... 56

4.2 Future Work………………..…………………………………………………… 57

REFERENCES…………………......………………………………………………… 60

APPENDICES

Appendix A Experimental Uncertainty Calculations... 64

Appendix B Measurement Results... 72

LIST OF TABLES

Tables

Table 1.1 Previous experimental studies on near field radiation measurement……….. 15

Table 2.1 Number of samples fabricated for different samples dimensions, wall thicknesses and gap eights………………………………………………. 22

Table A.1 Uncertainty calculations results…………………………………… 69

Table B.1 Measurement results……………………………………………… 72

LIST OF FIGURES

Figures

Figure 1.1 Illustration of evanescent or surface waves…………………………….... 2

Figure 1.2 Radiative heat transfer coefficient versus distance ....………….......... 4

Figure 1.3 Schematic of a TPV system …..….. 5

Figure 1.4 Hargreaves test setup and sample……………………………………….. 8

Figure 1.5 Experimental setup by Hu et al, 2008…………………………………... 9

Figure 1.6 Experimental Results……………………………………………………. 10

Figure 1.7 Ottens' experimental setup……………………………………………… 10

Figure 1.8 Measurement result showing heat flux enhancement Ottens et al, 2009.. 11

Figure 1.9 Experimental setup Xu et al, 1994……………………………………… 12

Figure 1.10 (a) Experimental Setup. (b) results (Kittel et al., 2005)……………… 12

Figure 1.11 (a) Experimental setup and (b) results of Naranaswamy et al…………. 13

Figure.1.12 Experimental results (Narayanaswamy et al., 2008)………………… 14

Figure 1.13 Near Field Radiative transfer work groups……………………………. 17

Figure 2.1 (a) SiO_2 wall deposition on Si wafer (b) wafer pair after bonding……... 21

Figure 2.2 Max deflection of simply supported 0.5 mm thick Si-Plate vs. width and length………………………………………………………………………… 24

Figure 2.3 Permeation, diffusion and desorption of gases through solids………….. 26

Figure 2.4 Permeability of He ,D_2, Ne, Ar and O_2 through silicon oxide glasses…. 26

Figure 2.5 Vacuum level vs. time inside the gap…………………………………… 28

Figure 2.6 Heat conduction through air inside the gap vs. separations between plates at 10^{-3} mbar ………………………………………................................... 29

Figure 2.7. Heat conduction through air inside the gap vs. pressure……………… 30

Fig 3.1 Fabrication process and facilities………………………………………….. 32

Fig.3.2 First and second oxidation processes……………………………………… 33

Fig. 3.3 Thermal oxidation furnace at METU-Central Laboratory Cleanrooms…… 35

Fig.3.4 Schematic of quartz tube…………………………………………………… 35

Fig. 3.5 Oxide thickness versus time graph for dry oxidation at 1100 °C………….. 36

Figure 3.6 One dimensional model for oxidation of silicon………………………… 37

Fig 3.7 (a) image of mask prepared with L-edit Pro software (b) patterns on wafer after etching image taken with optical microscope………………………………… 39

Figure 3.8 (a) Pattern replication on photoresist (b) photoresist removed with solvent (c) silica etched with chemical BOE (d) second oxidation process (e) bonding of patterned wafer and silica coated top wafer (f) sample after wafer dicing………………………………………………………………………….…...... 43

Fig 3.9 Bonded wafers with vacuum gap inside……………………………………. 44

Fig 3.10 Fusion bonding steps……………………………………………………… 45

Fig. 3.11 (a) C-SAM (b) C-SAM micrograph……………………………………… 46

Fig. 3.12 (a) Wafer dicer's blade (b) Wire cutter…………………………………... 47

Fig. 3.13 SEM micrograph of a diced sample……………………………………... 48

Fig. 3.14 SEM Separation between silica coated silicon wafer at at magnification (a) 18000X and (b) 120000X 49

Figure 3.15 Bonding qualities by inspection with C-SAM………………………… 50

Figure 3.16 Testing sample…………………………………………………………. 51

Figure 3.17 Test setup at Özyeğin University……………………………………… 52

Figure 3.18 Nextreme UPF4 Optocooler TM thermoelectric cooler. (1.5x2.5 mm^2 footprint) 52

Figure 3.19 Total heat transfer vs. difference in measured temperatures (d=100nm) 54

Figure 3.20 Total heat transfer vs. difference in measured temperatures (d=200nm) 55

LIST OF SYMBOLS / ABBREVIATIONS

A	area of membrane
AFM	atomic force microscope
C-SAM	C-mode scanning acoustic microscope
cBN	cubic boron nitrate
CVD	chemical vapor deposition
d	thickness of membrane
D	plate's flexural rigidity
E_{100}	modulus of elasticity for <100> oriented silicon plate
GÜNAM	The Center for Solar Energy Research and Applications
h	plate thickness
IC	integrated circuit
K	permeation constant
Kn	Knudsen number
l	plate length
MEMS	micro-electro mechanical systems
PVD	physical vapor deposition
q	permeation rate
SiO_2	silica

SiC	silicon carbide
SPhPs	surface phonon polaritons
SPV	solar photovoltaic
STM	scanning thermal microscope
t	vacuum lifetime
T_c	cold surface temperature
TEC	Thermo electric cooler
T_h	hot surface temperature
TPV	thermophotovoltaic
V	volume of vacuum gap
W_{max}	maximum deflection
UNAM	National Nanotechnology Research Center
Δp	pressure difference
λ_{max}	characteristic wavelength
α_{ra}	numerical factor dependent on ratio of length/width
v_p	Poisson's ratio

CHAPTER 1

INTRODUCTION

A relatively new radiative heat transfer mode, near-field radiation, has been discussed by various researchers since 1960's. Near-field radiation takes place when the separation between two surfaces is of nanometer size. A motivation for the study of near-field radiative transfer will be given in this chapter. Then a detailed literature review will be presented, and the objective of the thesis will be described.

1.1 MOTIVATION

In his article dated back to 1960, Richard Feynman stated that "As we go down and fiddle around with the atoms down there, we are working with different laws, and we can expect to do different things", "all of our devices can be mass produced so that they are absolutely perfect copies of one another" and "at the atomic level, we have new kinds of effects" [1].

Feynman inspired new direction to the scientists with his lecture "There is plenty of room at the bottom" in 1959 and attracted interest to the fact that materials at nano-

scale can exhibit different physical, chemical properties compared with respect to their bulk counterparts.

Nanotechnology definition according to the National Science Foundation of U.S.A is as follows:

“Nanotechnology is the understanding and control of matter at the nanoscale, at dimensions between approximately 1 and 100 nanometers, where unique phenomena enable novel applications” [2].

In the past few decades with the development of fabrication, measurement and imaging techniques at the nanoscale, it became possible to realize the theoretical works on nanotechnology.

As the fossil energy sources are being used for about a century they will not support us everlasting. New, less hazardous and renewable energy sources must be found and improve. Solar energy and producing energy from waste heat are promising technologies to overcome problems due to high energy consumption. It’s well known that world energy consumption increases every year and more effective sources are needed.

The goal in this study is related to the conversion of waste heat from high-temperature to moderate-temperature sources to a more useful form, such as electricity, using near-field radiative transfer principles. The mode of radiation changes from far-field to near-field with decreasing distance down to nanometer size. In both far- and near-field, energy transfer is with the electromagnetic waves. In the far-field only the propagating waves contribute to the energy transfer, whereas in near-field tunneling of energy due to oscillations of charges (plasmons) or vibrations of lattices (phonons) may add significantly to the net energy transferred. Overall, the emission of energy can be calculated from Planck’s law. However, in the near-field, because of the size effects, radiative heat transfer can exceed by few orders of magnitude that was predicted by Planck’s blackbody distribution.

Planck made an assumption that “the linear dimensions of all parts of space considered, are large compared with the wavelengths of the rays considered” [3]. Therefore the blackbody concept proposed by Planck is no more valid when the

typical dimensions of space, which include the size of the bodies and their distances of separation, are small compared to the wavelengths emitted.

In the near field, radiative heat transfer occurs with evanescent waves or surface waves. Conversely to propagating waves, which play role in far-field radiation, evanescent waves propagate only along the interface of two media and exponentially decay over a distance of about a wavelength [4] as illustrated in Figure 1.1.

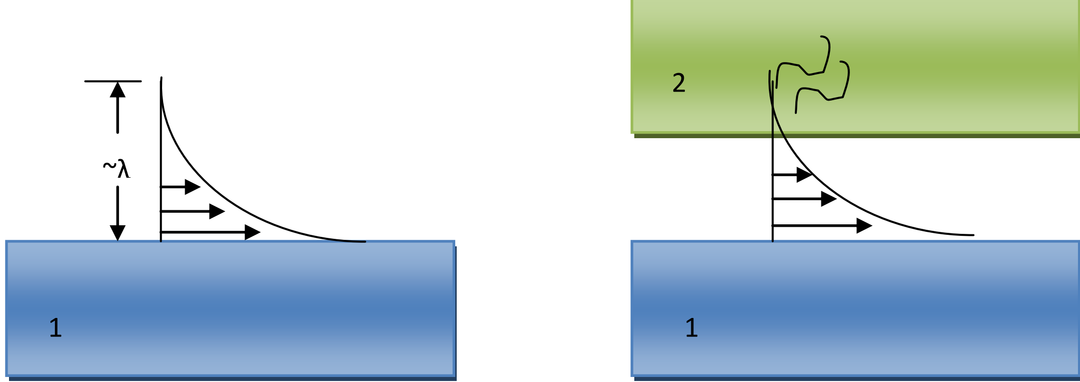

Figure 1.1 Illustration of evanescent or surface waves.

There can be net energy transfer in presence of a structure interacting with evanescent wave at distances below dominant or characteristic thermal radiation wavelength.

The dominant or characteristic wavelength can be calculated by Wien's displacement law:

$$\lambda_{\max} = \frac{2897.76}{T} \quad (1.1)$$

where T is the absolute temperature in Kelvin.

The total heat flux q between two parallel plates by considering the near field effects can be calculated by the integration of the difference of the oscillatory functions of the hot and cold plates multiplied by the weighing function X(ν) [5].

$$q = \frac{1}{\pi^2}\int_0^{\infty}\left[\Theta(\nu,T_h) - \Theta(\nu,T_c)\right]X(\nu)d\nu \quad (1.2)$$

Θ (ν) is Planck's oscillator defined by (1.3) where h is Planck's constant, ν is the frequency, K_b is the Boltzmann constant and T is the absolute temperature.

$$\Theta(\nu,T)=\frac{h\nu}{\exp\left(\frac{h\nu}{k_B T}\right)-1} \tag{1.3}$$

Equation (1.4) is the weighing function, which integrates the frequency dependent exchange function over the possible wave frequencies.

$$X(\nu)=\frac{4}{d^2}\int_0^{\beta_c}\frac{\varepsilon''(\nu)^2 e^{-2\beta}\beta d\beta}{\left|(\varepsilon(\nu)+1)^2-(\varepsilon(\nu)-1)^2 e^{-2\beta}\right|^2} \tag{1.4}$$

where d is the distance between plates, $\varepsilon(\nu)$ is the dielectric function, $\varepsilon''(\nu)$ is the imaginary part of the dielectric function and β is the parallel component of wave-vector to the surface. The dielectric function must be calculated based on the properties of the materials used. The preceding expressions indicate the enhancement in radiation heat transfer rate and $1/d^2$ dependence of the transfer coefficient due to the near-field effects [6]. Figure 1.2 shows this dependence.

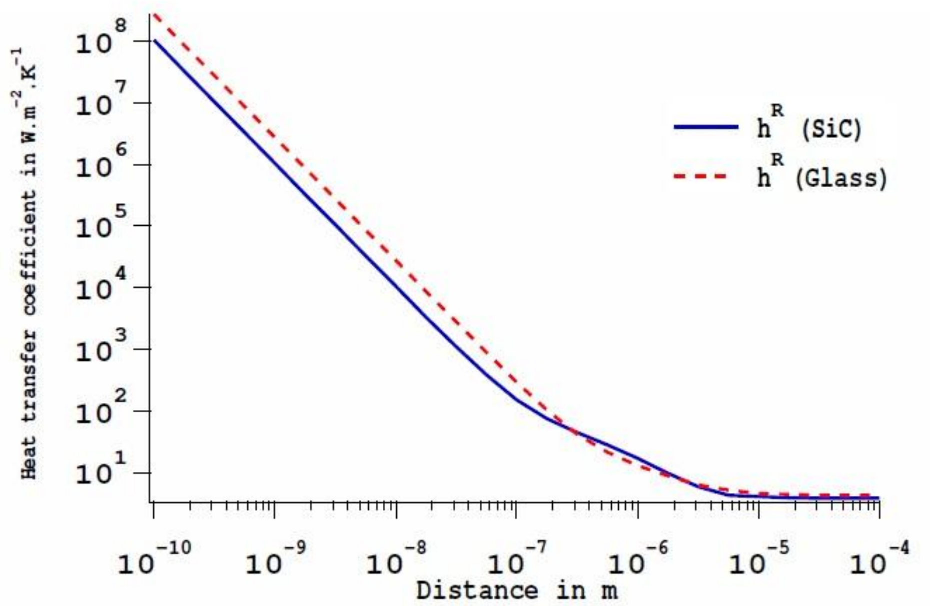

Figure 1.2 Radiative heat transfer coefficient versus distance [6].

Beside the enhancement of radiation heat transfer rate, near field radiation takes place in quasi monochromatic behavior due to possibility to high spatial and temporal coherences with surface polaritons in polar materials (photonic crystals: SiO_2, SiC, cBN) [4]. This quasi monochromatic behavior can be used as selective emitter in thermophotovoltaic (TPV) systems that utilize emissions in a narrow wavelength range for the energy conversion.

A TPV cell, just as solar photovoltaics (SPV), is a p-n junction of semiconductor which converts the electromagnetic energy radiated by a high-temperature thermal source into electricity.

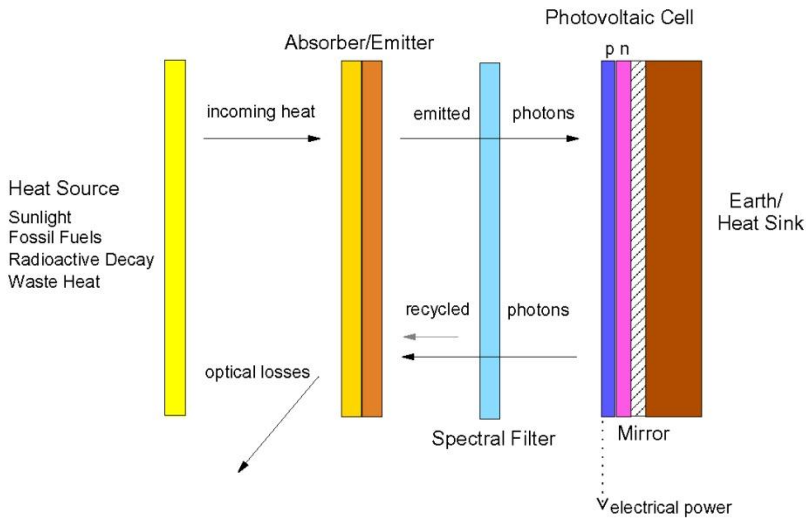

Figure 1.3 Schematic of a TPV system [7].

A generic TPV system; consists of a heat source, photovoltaic cell, selective emitter and/or filter. A schematic of a TPV system is given in Figure 1.3.

The main difference between SPVs and TPVs is the wavelength range of the conversion. The heat incident on a TPV is of a much wider spectrum, therefore filters and emitters are used to reduce the spectral width of the incoming photons to photovoltaic cell.

Photons with higher energy than the band gap energy of PV can generate electricity. The temperature of the thermal sources is typically in the range of 1000-2000 K. This corresponds to 0.6-0.9 eV radiant energy corresponding to 20.7μm and 13.8μm wavelengths [7]. The band gap of silicon photovoltaic is around 1.1 eV (11.3μm). Therefore less than 25% fraction of the incident thermal radiation has energy exceeding the energy band gap of a photovoltaic cell.

The efficiency of TPV is limited by this spectral mismatch between the emitter spectrum and the spectral response of the TPV cell. The photons with energy lower than the gap do not create electron-hole pairs and are responsible for heating the cell. On the other hand, for high-energy photons, the difference between photons energy and the energy gap is also lost in Joule heating [8]. Therefore, the ideal source for TPV conversion efficiency is a quasi mono-chromatic source at a frequency slightly higher than the gap frequency.

For this reason, closely spaced silica plates can be used as a selective emitter in TPV devices without a necessity for any filter.

Feynman also predicted possible new fabrication methods, which would be the basis of actual nano and micro fabrication methods [1]. With Micro-Electro Mechanical Systems (MEMS) fabrication methods it's possible to build structures down to sub-micrometers. With MEMS fabrication methods including deposition, lithography and etching techniques; several copies of a device can be printed on a single wafer and can be mass produced. The mass producing reduces the costs of fabrication.

Generally MEMS devices have usage in variety of areas in electronics. It is possible to fabricate combined sensors, actuators, vibrators, and many more mechanical structures in micrometer size. Devices fabricated with MEMS have higher durability, functionality and higher mechanical characteristics. MEMS fabrication enables possibility to combine mechanical and electronic systems together. In Turkey there is growing interest in MEMS fabrication. Some MEMS related facilities, research centers and workgroups in Ankara are METU-MEMS Center, Solar Energy Research Center (GÜNAM) of the Middle East Technical University, and the national nanotechnology research center (UNAM) located at Bilkent University.

Our objective in this thesis is to manufacture samples that can be used to understand and measure the near field radiative transfer between parallel plates separated by a gap of a few nanometers. The motivation is the further application of similar nano-structures in TPVs. Different stages of sample preparation took place at METU-Central Laboratories, METU-GÜNAM, Bilkent-UNAM in Turkey and EV Group laboratories in Austria. The samples have been tested in an experimental setup by a collaborative group at Özyegin University, İstanbul.

Below, first we will discuss different experimental works and outline experimental samples. After that a more detailed discussion of the work carried out during this study will be explained.

1.2 LITERATURE REVIEW

Theoretical studies on the enhancement of radiative heat flux between bodies of nanometer size have been carried out by various researchers. The theoretical studies in general are based on the fluctuating electrodynamics approach pioneered by Rytov *et al.* [9] and Polder and van Hove [10]. These theoretical studies show that when the distance between two parallel surfaces is small compared to the dominant thermal radiation wavelength, the near-field radiative heat flux can exceed the far-field upper limit proposed by Planck’s law of blackbody radiation. Besides the enhancement of the heat transfer rate, theoretical studies showed quasi monochromatic behavior in energy transfer via surface phonon-polariton coupling in thin films [12-19].

To verify theoretical foundations in near field radiation, experiments have been performed by limited number of researchers. The experimental setups were categorized based on the geometry of the samples as plane to plane, tip to plane and sphere to plane.

The first experimental study for the measurement of near field heat transfer was set up by Hargreaves in 1969 at Philips Company laboratories, Netherlands [20]. In this work sample was 5 cm^2 glass plates coated with 100 nm chromium. Measurements were performed in a vacuum environment of 10^{-5} torr to reduce the convection heat

transfer effects between plates. Piezo-electric ceramic pillars placed between the two plates were used for adjusting the spacing and the flatness of plates. All experiments were performed with high temperature, T_h , of 323 K and a low temperature, $T_{c,}$ of 306 K (See Figure 1.4). The minimum distance achieved between plates was 1.5 µm. The results showed 50% enhancement of blackbody radiation between two chromium surfaces.

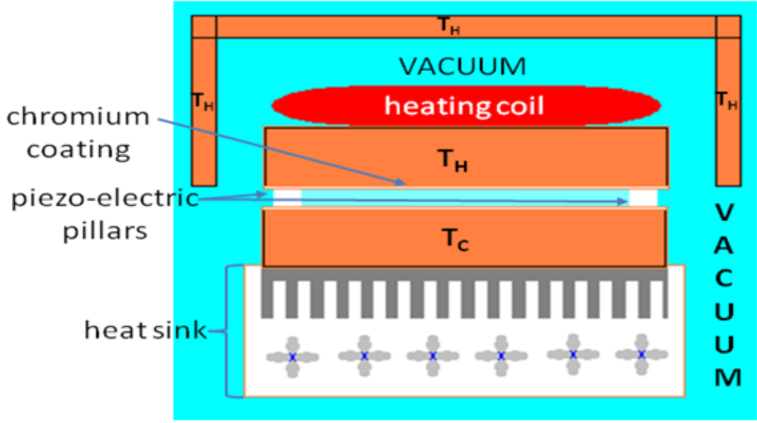

Figure.1.4 Hargreaves test setup and sample [20].

The experiments performed, by Domoto et al. (1970) at cryogenic temperatures were very similar to the experiment performed by Hargreaves. Two 8.5 cm diameter solid copper plates were used for the emitter and receiver. Piezo-electric devices were used as the adjustable supports. The experiments took place in a vacuum environment at 10^{-12} Torr. The receiver temperature T_c was held at 4.5 K while the emitter temperatures were 10 K, 13.8 K or 15.1 K. The minimum distances between plates achieved for this experiment was 10 µm. Measurements have been done at cryogenic temperatures to have longer dominant wavelengths. The dominant wavelength is 290 µm for 10 K so experiments took place in the near field. Although a small enhancement was observed in heat flux, there was inconsistency and uncertainties in the measurements [21].

Another experimental study was carried out by Hu et al. (2008) showing the near field enhancement between plane parallel glass surfaces (Figure 1.5). Glass was chosen due to its surface phonon polariton (SPhP) resonance in the infrared region of spectrum (for 300 K, approximately 10 µm). The resonance wavelength for metals is

smaller, thus emitter plate must reach higher temperature and distance between plates must be very low with respect to glass. Hot side and cold side temperatures 50 and 24°C (Hot and cold sides temperatures are 50°C and 24°C respectively) which correspond to 8.7 and 20.2 μm which are resonance wavelengths of SPhP's in glass [22].

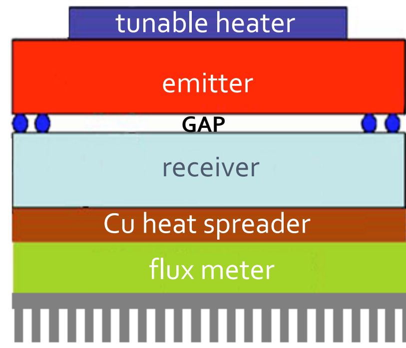

Figure 1.5 Experimental setup by Hu et al, 2008 [22].

Emitter and receiver glass plates have 5 cm^2 area and 0.635 cm thicknesses. The spacing of the plates was set to 1 μm using polystyrene spheres which have low contact area due to their shape and low heat conductance that limit the conduction heat flux to less than 2% of total heat flux. The experiment was carried out in a vacuum chamber at a pressure of $8.5x10^{-3}$ Pa.

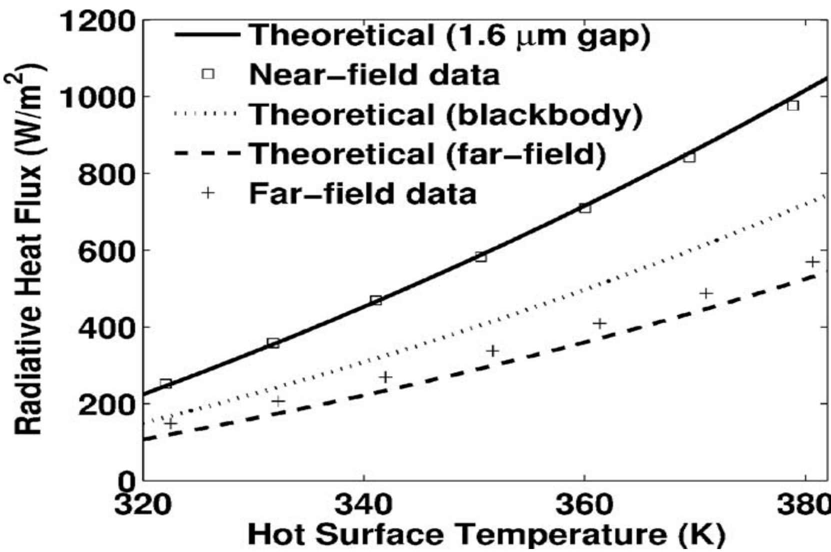

Figure 1.6 Experimental results[22].

The measured radiative heat flux in this experimental setup is reported to exceed the blackbody radiation by more than 35%.

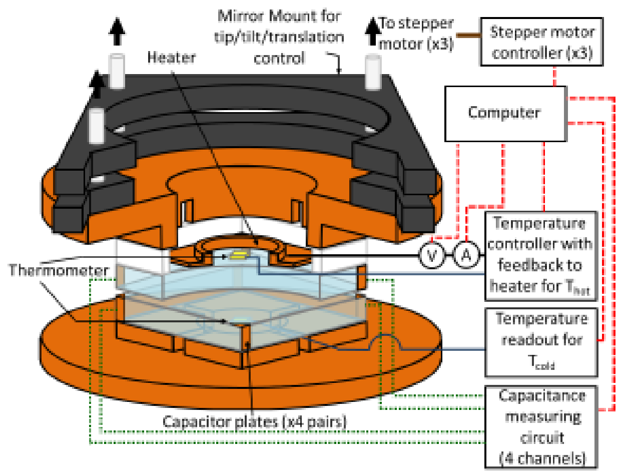

Figure 1.7 Ottens' experimental setup [23].

The most recent experimental study of near field heat transfer was conducted by Ottens et al. [23]. In this work, radiative heat transfer between 50x50x5 mm^3 sapphire parallel plates with separations between 2 – 100 μm was measured. Controlling plate separation and parallelism were maintained by capacitance measurements across the copper coated corner areas of plates. Stepper motors (35 nm steps) were used to adjust the separation between plates and equalize the four

capacitances. Plate temperatures were monitored using silicon diode thermometers deposited on top of the top plate and bottom of the bottom plate. The experiment took place in ultra-high vacuum conditions from 5×10^{-7} to 2×10^{-7} Torr. The same measurement was done for four different temperature combinations. These data agree with the theory of near field radiation enhancement by Polder and Van Hove (Fig 1.8).

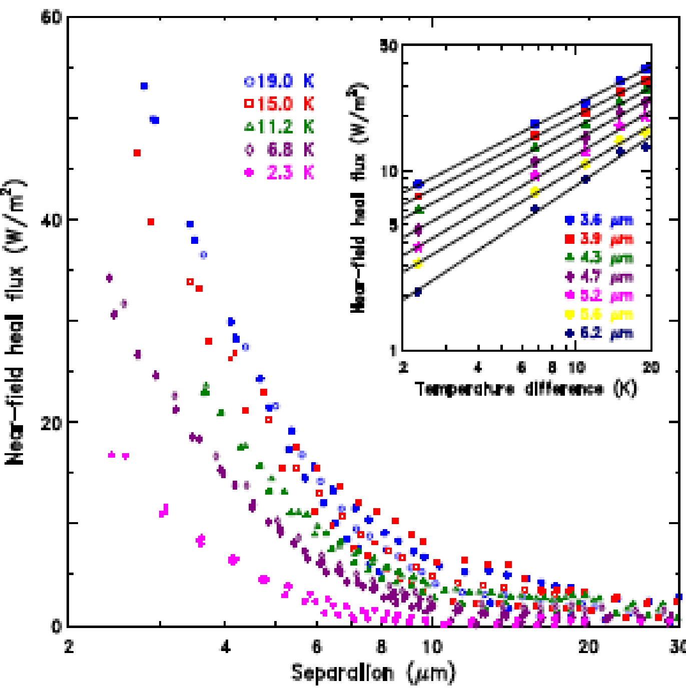

Figure 1.8 Measurement result showing heat flux enhancement [23].

In 1994, Xu *et al.* [24] tried to measure near-field radiative heat transfer through a sub-micrometer vacuum gap by using an indium needle of 100 μm diameter and a thin-film thermocouple on a glass substrate, but could not observe a substantial increase of radiative heat transfer. The experimental setup is shown in Figure 1.9.

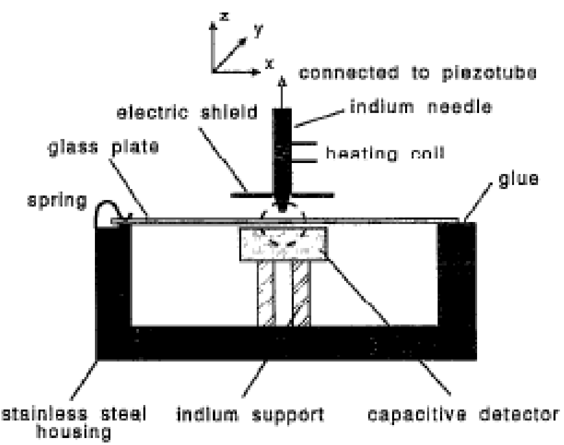

Figure 1.9 Experimental setup by Xu et al, 1994 [24].

Scanning thermal microscope (STM) was used for the measurement of heat flux between gold (Au) or gallium nitride (GaN) surfaces with the tip of microscope under ultra-high vacuum. Using STM allowed a very fine adjustment of tip to plane spacing, on the order of 1 nm. The temperatures of flat surface and the tip was 200 K and 100 K, respectively [25].

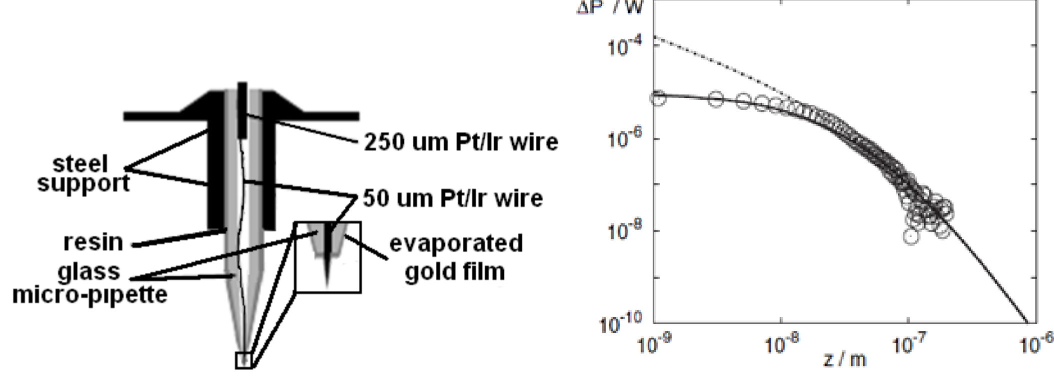

Figure 1.10 (a) Experimental Setup. (b) results (Kittel et al., 2005)

The results of this experiment showed that heat transfer rate between tip and surface deviates for sub- 50 nm distances from those predicted by fluctuational electrodynamics as may be seen in Figure 1.10 b, where dashed line represents the predicted flux using fluctuating electrodynamics and small circles correspond to experimental data.

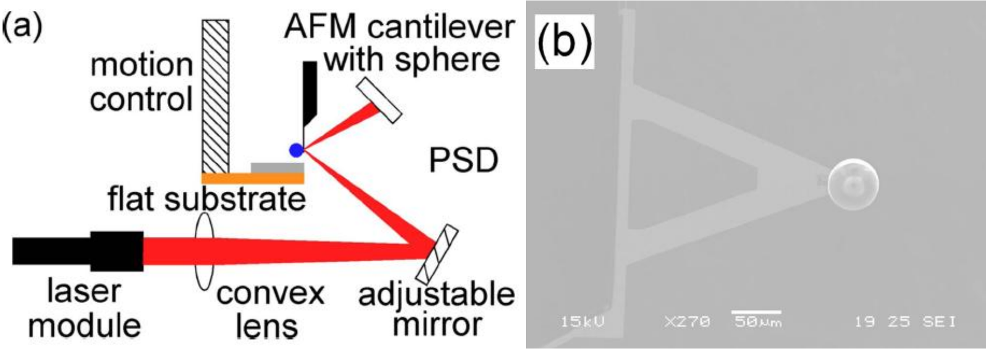

Figure 1.11 (a) Experimental setup and (b) results of Naranaswamy et al. [26].

Another experiment was done by Narayanaswamy et al. (2008) [26] with a silica sphere of diameter 50 µm. Silica to plane geometry is shown in Figure 1.11.

AFM bi-material cantilever, which bends in response to temperature gradients in the cantilever, is used as thermal sensor with minimum detectable power of $5x10^{-10}$W. The test setup is placed in a vacuum chamber pumped down to $6.7x10^{-3}$ Pa. Figure 1.12 presents radiation transferred via the near-field effect measured at a distance of approximately 9 µm. The maximum measured conductance was 6 nW/K above the Planck limit of 29 nW/K for a blackbody that represents near-field enhancement by 17% (Figure 1.12).

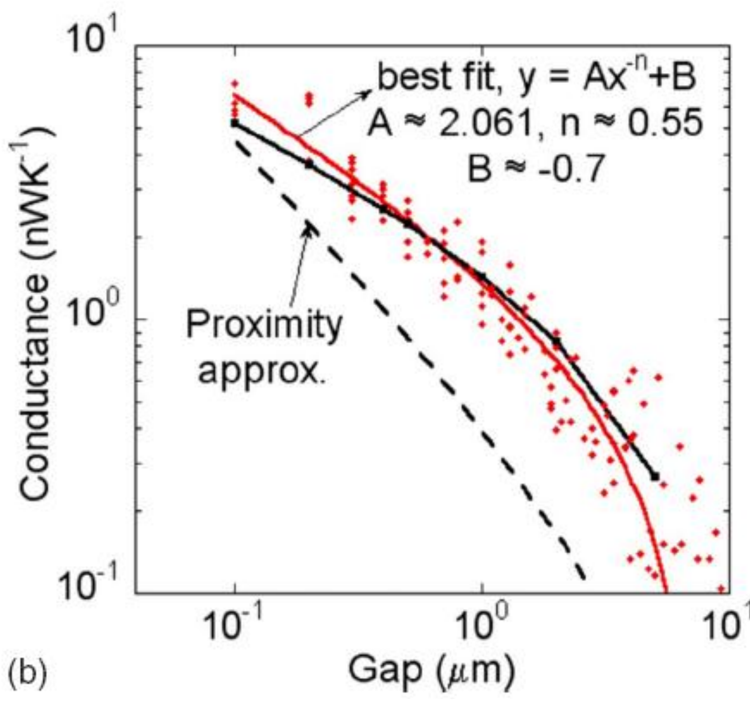

Figure.1.12 Experimental results (Narayanaswamy et al., 2008).

Previous experimental studies on the measurement of heat flux in the near field have been conducted between various materials (dielectrics, metals) with different geometries (plane to plane, sphere to plane and tip to plane) [20-26]. The measurements of the enhancement in the heat flux between dielectric materials were more convenient due to coupling SPhPs' at temperatures in range of the interest. The experiments were desired to be performed at minimum gaps down to a few nanometers. The experiments were performed by using AFM and STM which have very precise distance control systems [25, 26]. For planar surfaces, the minimum gap was around 1 μm [20-23]. The distance was determined by step motors and piezo electric materials for plane to plane experiments. Capacitance measurements were utilized to measure distance and flatness of planes. All experiments have been conducted in vacuum chambers. Table 1.1 summarizes the major characteristics of previous experimental studies.

Table 1.1 Previous experimental studies on near field radiation measurement

Experiment	Sample	Dimensions	Operation temperature	Vacuum condition	Minumum distance	Geometry
Hargreaves 1969	chromium coated glass	5 cm^2	T_h 323 K T_c 306 K	Chamber 10^{-5} torr	1.5 µm	plane to plane
Domoto 1970	solid copper plates	8.5 cm diameter	13.8 K 15.1 K	10^{-12} Torr	10 µm	plane to plane
Hu et al. 2008	Glass plates	5 cm^2	24°C 50°C	8x10^{-5} Pa	1 µm	plane to plane
Ottens et al. 2010	Glass plates	25 cm^2	327 K-308K 322K-307K 317K-305.8K 312K-305.2K	2x10^{-7} Torr	2 µm	plane to plane
Kittel et al. 2005	Au tip GaN surface	-	200K-100K	Ultra High Vacuum	1 nm	tip to plane
Narayanaswamy	Silica sphere to surface	50 µm	ΔT 50 K	6.7x10^{-3} Pa	5 nm	sphere to plane

1.3 OBJECTIVE OF THE THESIS

Previous studies or experiments on near field radiation were done at “ideal conditions” at laboratories and in vacuum chambers with separations between object and flatness of plates were controlled with appropriate systems (AFM, piezo electric materials and capacitors). They were mostly focused on the measurement of the near field effects, and compared experimental results with theoretical calculations. The measurements showed an enhancement in the heat flux as the gap decreases to a few nanometers.

This work is a part of a joint study which consists of preparing samples and measurement of near field heat flux by establishing a test setup. A detailed collaboration map is given in Figure 1.13.

The present work aims to prepare compact and individual wafer sandwiches that can be tested and quantified in test setup and can be mounted for other devices such as TPV’s.

Samples with 1×1, 2×2 and 5×5 mm^2 surface areas, and with 25 nm, 50 nm, 100 nm and 200 nm (nano-gap) separations have been fabricated by MEMS fabrication methods.

Fabrication has been performed in four stages at four different facilities. Thermal oxidation took place at the Central laboratory, METU. Samples have been patterned and chemically etched at UNAM, Bilkent University. Wafer pairs have been bonded at EV Group company laboratories in Austria to get a 3D structure, and diced at UNAM and GÜNAM to get individual samples. Finally samples were tested in the test setup established by Kurt Webb at Özyeğin University.

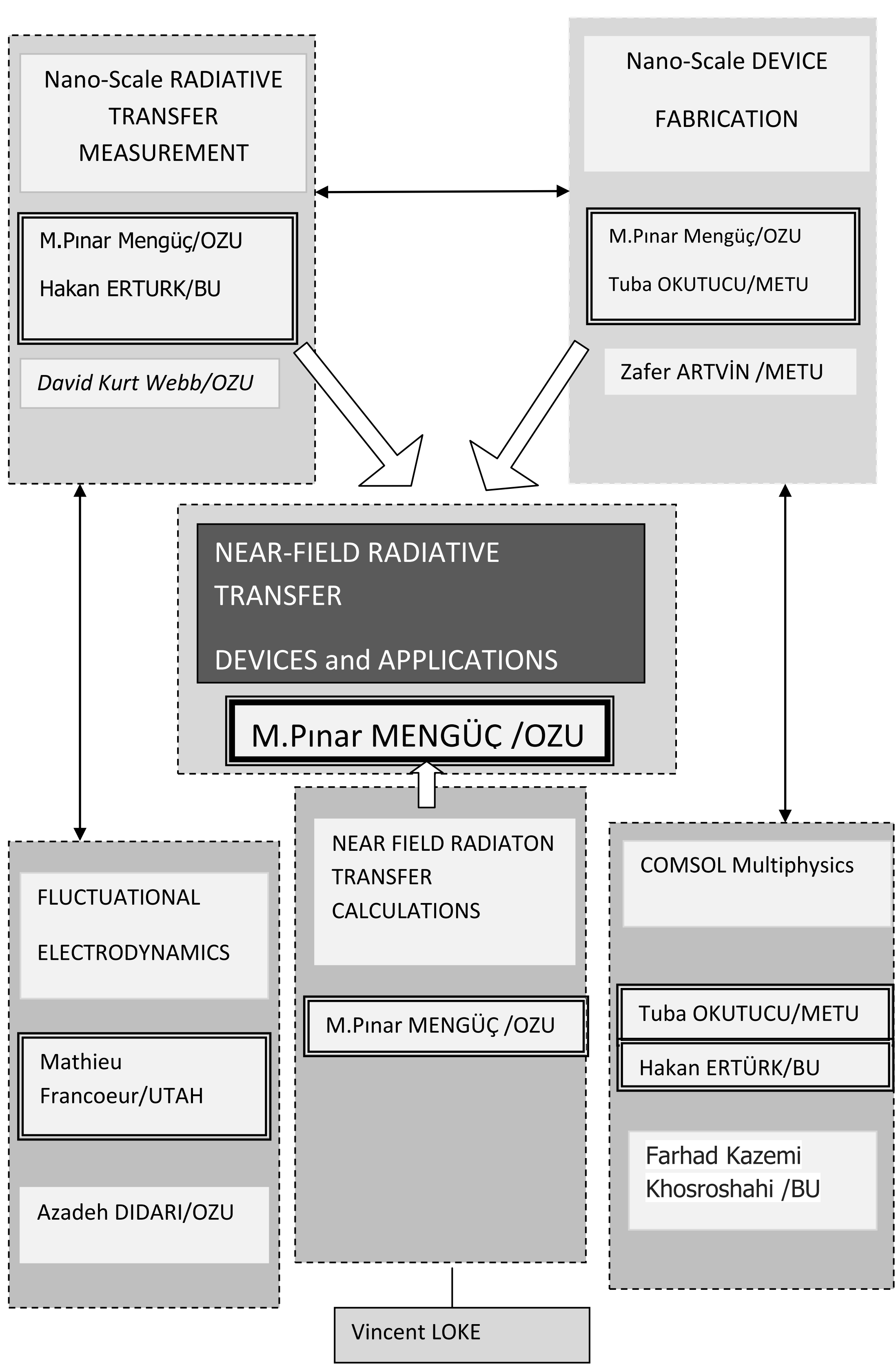

Figure 1.13 Near Field Radiative transfer work groups

CHAPTER 2

SAMPLE DESIGN

Before the fabrication stage, the dimensions of the samples, the materials to be used, and the fabrication methods have to be decided. The allowable sample dimensions are limited by the fabrication constraints, and have to be determined so as to provide the maximum possible radiation to conduction heat transfer ratio. The materials have to be selected for the maximum contribution to the enhancement of near-field radiative heat transfer. Reachable facilities, equipments and compatible fabrication methods have to be chosen. The design should be made to prevent the deflection of the parallel surfaces to avoid touching of them. Vacuum should be maintained inside the samples for a reasonable period of time. In this chapter, the design stage is described in detail.

2.1 MATERIALS

2.1.1 SILICON WAFER

Silicon wafers have common usage in MEMS technology. They are produced by thin slicing of single crystalline silicon. 4 inch diameter, 500 µm thick silicon wafers with both sides polished have been used to minimize the roughness. Crystal orientation of

wafers were <100> with n type dopant. Silicon wafers were provided by UNAM from Cemat Company.

2.1.2 SiO_2

SiO_2 has common usage as electrical isolation, mask against dopants and surface passivator in MEMS technology. There are various techniques (CVD, PVD and oxidation) to obtain a silica (SiO_2) layer.

A thin silica layer is deposited by dry oxidation in a thermal oxidation furnace over both silicon wafers to obtain a thermally poor conductor surface (k_{silica} = 0.014 W/m·K) [16]. Therefore, the silica layer was obtained to decrease the ratio of conduction heat transfer to total heat transfer. Silica layer which has been obtained with dry oxidation has better material characteristics such as higher density, and lower surface roughness. The density and surface roughness of silica layer are important for better bonding quality. An additional annealing step has to be done after oxidation methods such as wet oxidation or physical vapor deposition (PVD).

Radiant surfaces between plates are silica, which is a photonic crystal, supporting surface phonon polaritons (SPhPs) in the infrared region of electromagnetic spectrum. The resonant wavelength of SPhPs in SiO_2 is well aligned with the peak wavelength of thermal radiation in the temperature range of interest (for 300 K approximately), leading to higher radiative heat transfer even with moderate gap sizes [17]. When SPhP's thermally are excited, near field radiative transfer becomes quasi monochromatic. This quasi monochromatic behavior is important for thermophovolvaic generators where the objective is to maximize radiative fluxes in a narrow spectral band. The SPhP resonance for metals occurs at much lower wavelengths. Therefore, it is much easier to observe near-field enhancement in glass or other polar SPhP supporting materials.(photonic crystals) than metals [18].

As discussed in section 2.3.2 diffusion rate of gases through silicon (Si) wafer is much higher than through silica (SiO_2). Therefore, in order to get a better lifetime for vacuum inside the gap silica should be chosen.

In addition to having preferred and functional material properties, silica as mentioned above has common usage in IC technology and easier to utilize compared to other photonic crystals (SiC, cBN).

2.2 SAMPLE DESIGN

For the heat flux measurements between closely spaced plates, silicon wafer sandwiches have been designed as shown in Figure 2.1.

The dimensions of samples, materials and separations between plates have been arranged for getting the maximum possible near field radiation heat transfer. As the area of plates to wall thicknesses ratio increases the rate of radiation heat transfer increases. Therefore, samples with different plate area and wall thicknesses have been designed.

Besides, fabricational limits for production, compatibility of samples with the test setup and some physical effects (deflection, vacuum lifetime) on samples have been taken in to account.

3-D samples have been fabricated using MEMS production methods. The samples have vacuum gaps in between the two silicon wafers, each coated with a thin silica (SiO_2) film. The gap height is on the order of a few nanometers, and may be adjusted by controlling the oxide thickness. The vacuum gap is surrounded by silica walls.

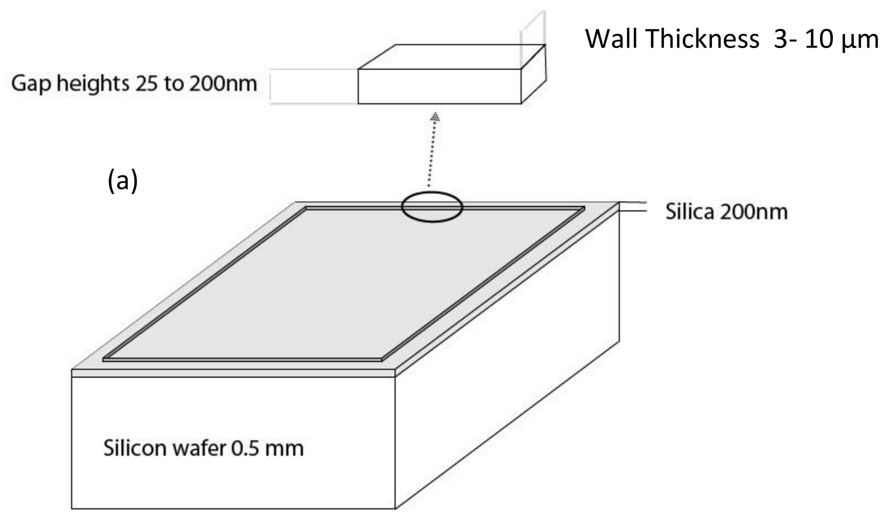

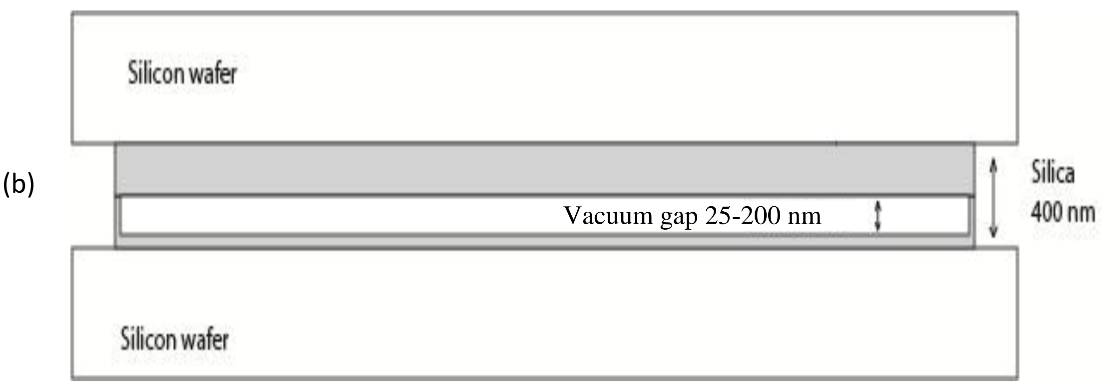

(c)

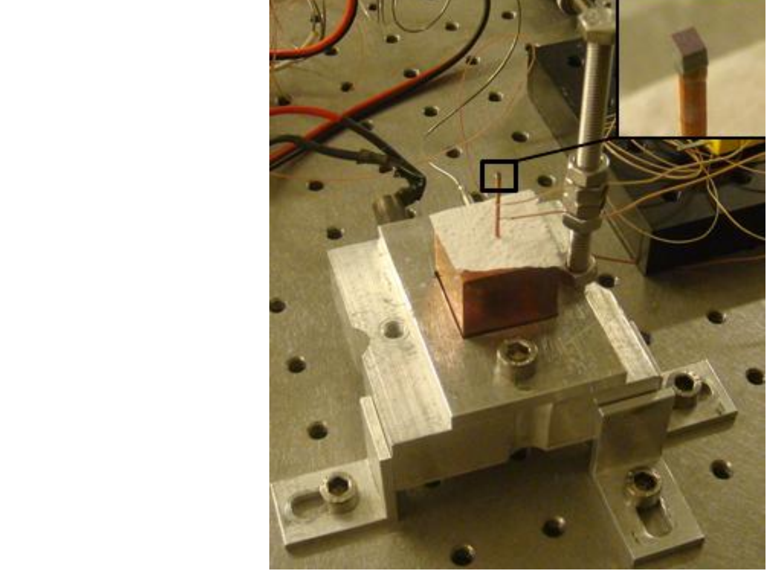

Figure 2.1 (a) SiO_2 walls on Si wafer (b) wafer pair after bonding. (c) 1x1 mm^2 sample.

Over one hundred sets of samples with varying dimensions have been fabricated. The dimensions of the samples in each set are summarized in Table 2.1. By varying sample dimensions (1x1, 2x2, 5x5 and 19x19 mm^2) and the wall thickness (1.2, 1.5, 2, 3, 5 and 10 µm), heat transfer rates and structural properties have been tested.

Table 2.1 Number of samples fabricated for different samples dimensions, wall thicknesses and gap heights

	Sample dimensions width x length (mm^2)									
	1x1						2x2		5x5	19x19
Gap Height	Wall thicknesses (µm)									
	1.2	1.5	2	3	5	10	1.5	2	2	3
25	10	20	20	20	10	10	4	4	8	2
50	10	20	20	20	10	10	4	4	8	2
100	10	20	20	20	10	10	4	4	8	2
200	10	20	20	20	10	10	4	4	8	2
Red: Touching surfaces Green: Available Navy: Tested Dark Green: Diced and sent for test										

As the wall thickness increases, better bonding quality and better vacuum lifetime is obtained, however, the rate of conduction heat transfer against radiation also increases. In order to minimize conduction, walls as thin as possible are required. Variable vacuum gaps (separation between plates) show the influence of the distance between silica coated plates on the heat flux. The theory of near field heat transfer presents increasing in the transfer rate as the separation decreases.

Dimensions of samples have been arranged according to the theoretical foundations (wall thicknesses must be as thin as possible and separation must be lowest) and fabricational limits. Wall thicknesses under 1.5 µm could not be printed on the wafer

because of the limitation of optical lithography machine. Besides, during the etching process corrosion effect of the chemical (BHF) on the wall may etch too thin walls.

The fabricated samples are compact, reproducible and may be mounted on other devices for further applications. A top down approach has been followed for the production. Thermal oxidation has been employed for the silica layer deposition, and optical lithography is utilized for printing the structures on the silicon wafers. Finally, a 3D structure has been obtained by wafer bonding to encapsulate the vacuum gap. The bonded wafers are then diced into the sample chips for the heat transfer experiments.

2.3 DESIGN CALCULATIONS

2.3.1 DEFLECTION

Deflection is one of the most important design issue for fabrication due to the risk of touching of the two plates to each other. The pressure difference between the inner vacuum gap and the surrounding environment at atmospheric pressure can cause the bending of the plates towards the gap. This may result in the contact of the parallel plates. If the two plates touch each other there will be conduction rather than radiative transfer. Because of this critical role, deflection calculations have been made by D. Kurt Webb [44] during the design period.

According to these calculations, the gap reduction for 1x1 mm^2 samples is less than 1% at the point of highest deflection. So it was decided that the deflection in this case will not greatly affect the flatness and gap uniformity.

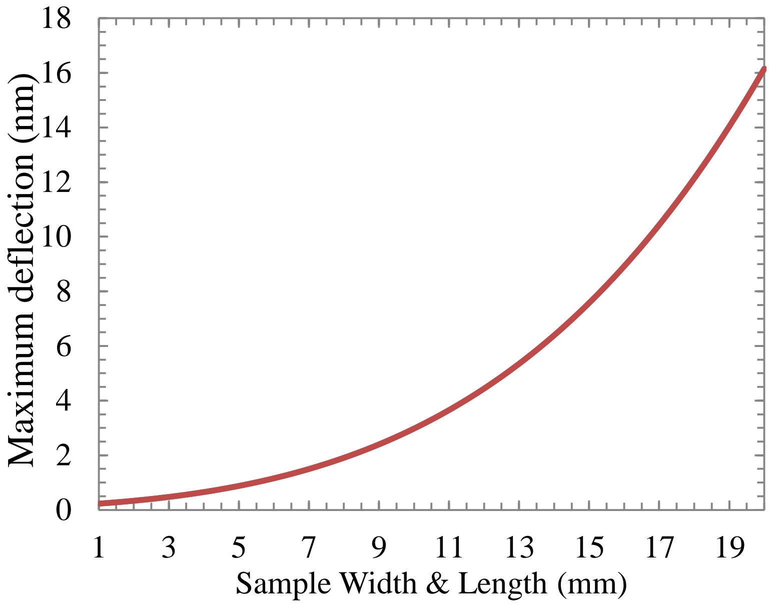

Figure 2.2 Maximum deflection of simply supported 0.5 mm thick Si-Plate vs. width and length [44].

However, for the samples with length and width of 19x19 mm^2 the maximum deflection is calculated to be 12.7 nm corresponding nearly 50% decrease of distance for samples of 25 nm vacuum gaps. Although it would contribute the conductive heat transfer, pillars were placed at the centers of 5x5 and 19x19 mm^2 samples to reduce the deflection effects.

The touching of wafer surfaces for any gap heights and dimensions were not expected according to the deflection calculations. However, by inspection with C-SAM microscope, which has taken images after the bonding of wafers, it can be seen that all 19x19 and 5x5 mm^2 samples collapsed and plates touched each other. The reason for the touching of the wafers is thought to be that because of the high mechanical pressure (10,000 N), exerted during the wafer bonding, which broke the thin walls between the surfaces.

2.3.2 VACUUM LIFETIME

To get vacuum inside the gap was important for heat flux measurements (To have a vacuum filled gap is important for heat flux measurements) . All theoretical calculations in near field assumed that vacuum present is between the radiant and absorber surface. Because of the fact that if the vacuum is over 0.1 Pa radiation will no longer be the dominant heat transfer mode [11], and convection heat transfer would be more effective. Experimental studies up to now have been performed in vacuum chambers in laboratory conditions. In our study, vacuum is formed and sealed in the gap by the wafer bonding equipment (EVG 520IS Semi-Automated Wafer Bonding System) which has vacuum chamber at a pressure of 10^{-3} mbar at EVG, Austria laboratories. The fabricated samples, which hold vacuum inside, may be mounted later on different devices especially on a TPV cell.

After wafer bonding and trapping vacuum inside, the critical point is the vacuum life time. As discussed above, samples have very thin walls and gaps between plates have tiny volumes, which are thought to make it harder to hold the vacuum for a long time.

Leakage and outgassing can affect the vacuum life time and quality during and after fabrication of samples. Cracks, voids or spaces between wafers in unbounded areas can cause leakage resulting in immediate loss of vacuum. Outgassing is the releasing of a gas from the inner walls of the gap that hold under vacuum. Two main factors contribute to the outgassing rate:

1- Desorption: Chemically or physically bound gases or contaminations from a previous fabrication process at the surface of inner walls can desorb under vacuum condition.

Wafer bonding has been done in vacuum chamber and the surfaces of wafers have been cleaned using a mega-sonic cleaning nozzle. Therefore, the desorption of gases from inner surfaces were thought to be non-effective.

2- Permeation: Gas permeation through the walls is a multi-stage process. Gas absorbed and dissolved from the outer walls, diffuses through the material and desorbs from the inner walls of the gap as shown in Figure 2.3.

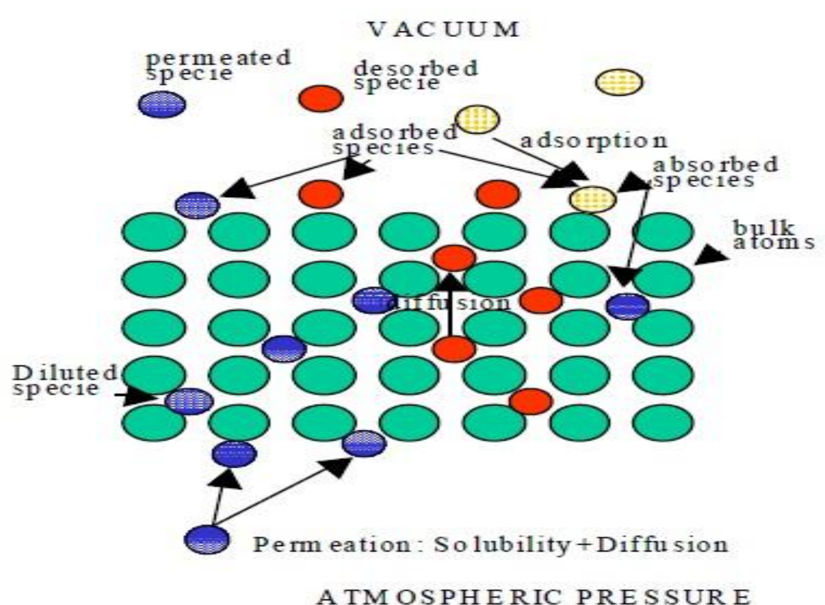

Figure 2.3 Permeation, diffusion and desorption of gases through solids [43].

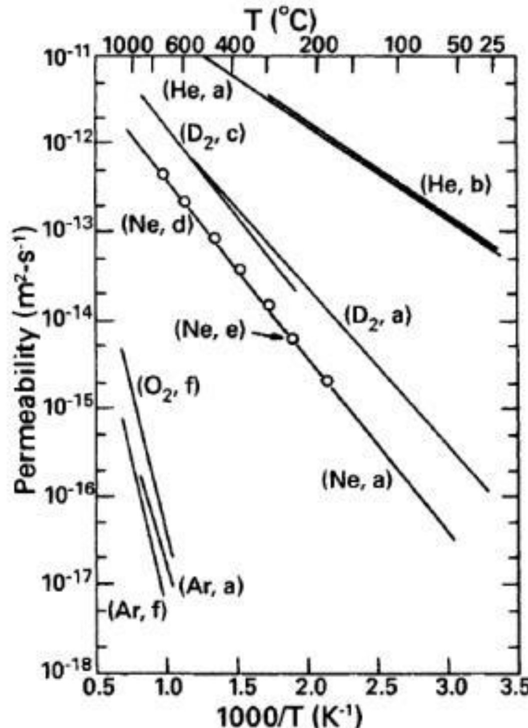

Figure 2.4 Permeability of He , D_2, Ne, Ar and O_2 through silicon oxide glasses[24].

Permeation rates of gases depend on non-perfect density of solids due to defects, internal porous structure and chemical affinity of a gas for solid. Some gases can interact with solids when passing through, thereby slowing down the diffusion. Permeation rate decreases with decreasing temperature [31].

The data for permeation rates for some gases (N_2, H_2, Ar, O_2) through SiO_2 were not available at room temperature. Since, our samples were kept and measurements conducted at around room temperature, permeation rates of these gases have not been taken in to account. Although helium has maximum diffusion rate of through SiO_2 (10^{-9} atm-cc/sec) at 25ºC, presents at very low percentage in air by 0.0005%. Nitrogen, which constitutes 78% of air mixture, has a permeation rate of 10^{-14} atm-cc/sec at 1300°C. Therefore, the most effective gas for the vacuum inside the gap is considered as oxygen which has a permeation rate of 10^{-11} atm-cc/sec at 1300°C and constitutes 20% of air.

The permeation rate of a gas through a solid may be calculated as:

$$q = \frac{K.A.\Delta P}{d} \tag{2.3}$$

Where K, A, Δp and d correspond to permeation constant (atm-cm^3/sec), area of membrane (cm^2), pressure difference (atm), and thickness (cm), respectively. To calculate the lifetime for vacuum in the gap, the volume (V, cm^3) and permeation rate (q) should be taken into account. For every 2% pressure difference time was plotted until equivalent pressures are maintained inside the gap and environment as shown in Fig.2.5.

$$t = \frac{V}{q} \tag{2.4}$$

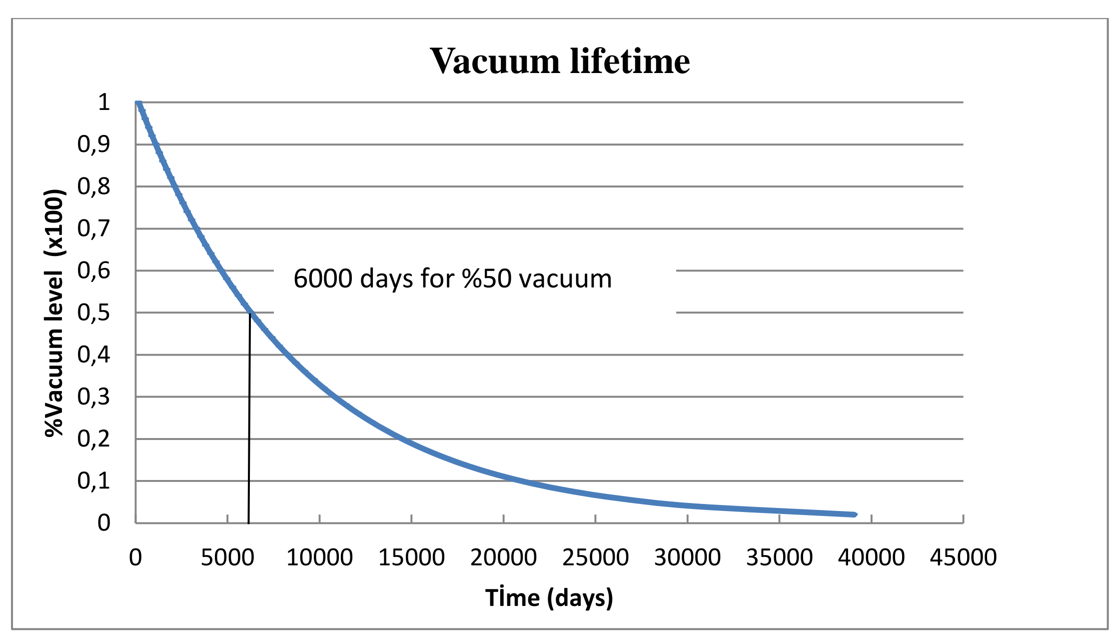

Figure 2.5 Vacuum level vs. time inside the gap. Oxygen permeation at 1300°C in air ambient.

Based on the calculations the gas permeation through our samples' walls has been neglected at room temperature. Results showed over 15 years duration to lose half of the vacuum percentage at 1300°C.

The vacuum level inside the gap could not been characterized by an appropriate measurement system. According to our estimations desorption and permeation are not very effective. If the wafers are successfully bonded without any leakage due to voids and cracks, holding vacuum inside the gap would be sufficiently long.

2.3.3 CONDUCTION HEAT TRANSFER THROUGH AIR INSIDE THE GAP

Conduction heat transfer through air between 1x1 mm^2 samples has been calculated to investigate its contribution to the total heat transfer.

First the Knudsen number, *Kn*, is determined in order to decide on the calculation method.

$$Kn = \Lambda / L \tag{2.5}$$

The continuum regime is no longer valid when one of the geometric dimensions, called characteristic diemension $L_{c,}$ is comparable to the mechanistic length, such as mean free path Λ [35]. For our pressure level and dimensions; Kn >> 1 and the free molecule regime should be considered for the calculations. Then,

$$q = \frac{k(T_1 - T_2)}{L(1 + Kn\, X)} \tag{2.6}$$

where k is the effective thermal conductivity, L distance between parallel plates of temperatures T_1 and T_2, X is a function that includes the effects of thermal accommodation coefficient of air to silica $\alpha_{t,}$ and specific heat rate γ (c_p/c_v).

The calculations have been carried out for the pressure of 10^{-3} mbar which is the pressure at which the bonding took place. Heat conduction rates between the plates for a variety of gap separations are presented in Figure 2.6.

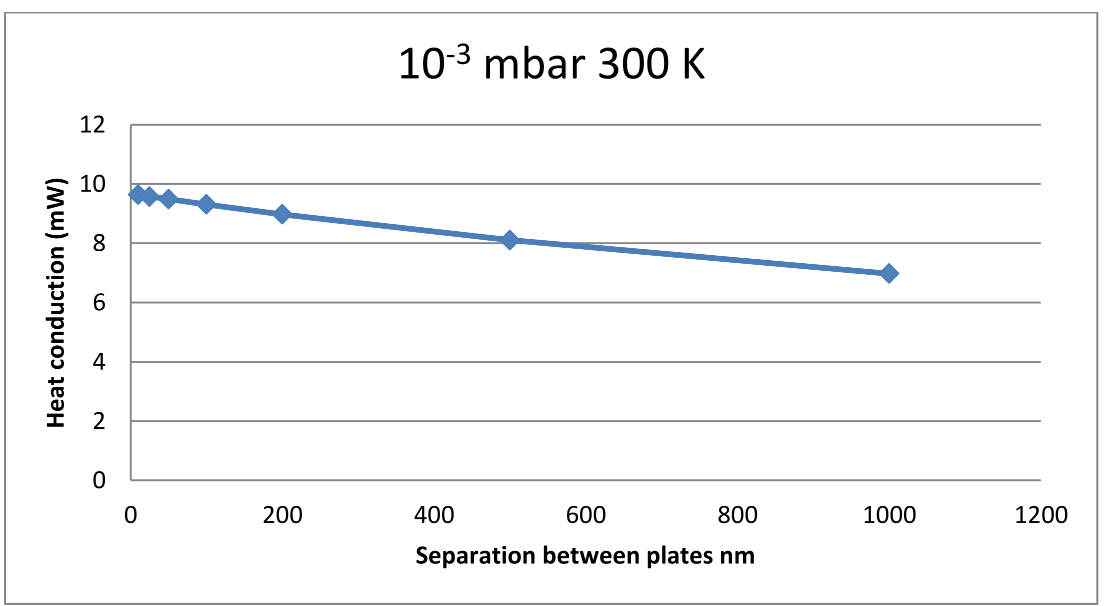

Figure 2.6 Heat conduction through air inside the gap vs. separations between plates at 10^{-3} mbar.

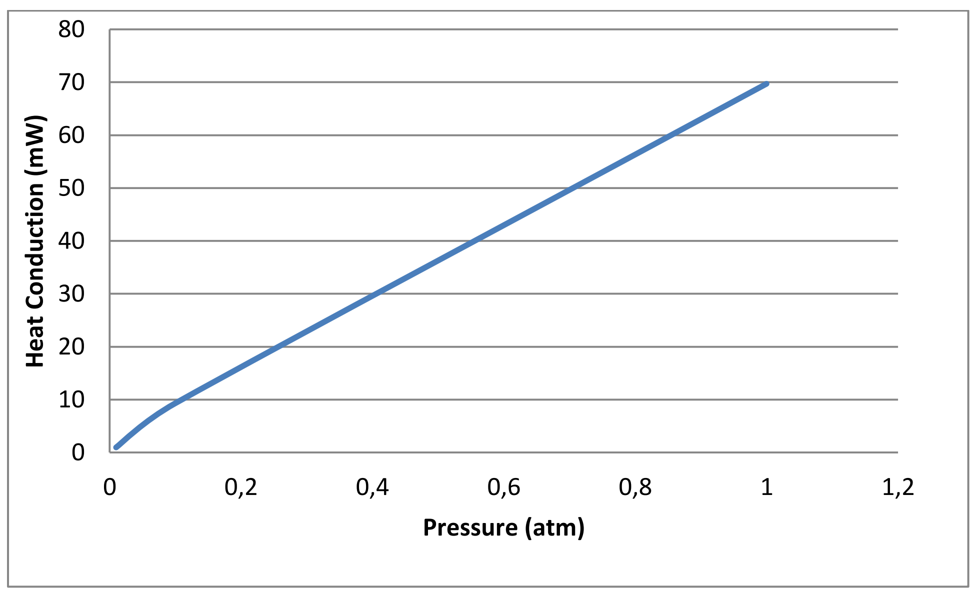

Figure 2.7 Heat conduction through air inside the gap vs. pressure between plates

The contribution of conduction increases as the air pressure inside the gap increases as shown in Figure 2.7.

The total heat transfer rate through the gap may be measured experimentally. Figure 2.7 indicates that while estimating the contribution of conduction to the total heat transfer, the effect of pressure inside the gap should be considered.

CHAPTER 3

SAMPLE FABRICATION

This chapter describes the fabrication steps in detail. A discussion on the quality of the fabricated samples is also given. Finally, the results of the tests with the fabricated samples have been presented.

3.1 FABRICATION STEPS

It is possible to describe the fabrication process in four different phases:

1. Oxidation of the silicon wafers,
2. Optical mask preparation, lithography and etching,
3. Wafer bonding,
4. Dicing.

Details of each phase will be given next.

In the Figure 3.1 fabrication steps are shown. Four different facilities have been employed including UNAM, METU-CENTLAB, GUNAM, EVG Company. Thermal oxidation furnace in METU Central Laboratory clean room was used for dry and wet oxidation. Mask preparation, photolithography and etching processes have been done at Bilkent UNAM clean rooms. Wafer bonding has been performed

at EVG Company in Austria by their technicians. Wafers have been diced in both UNAM and GÜNAM facilities.

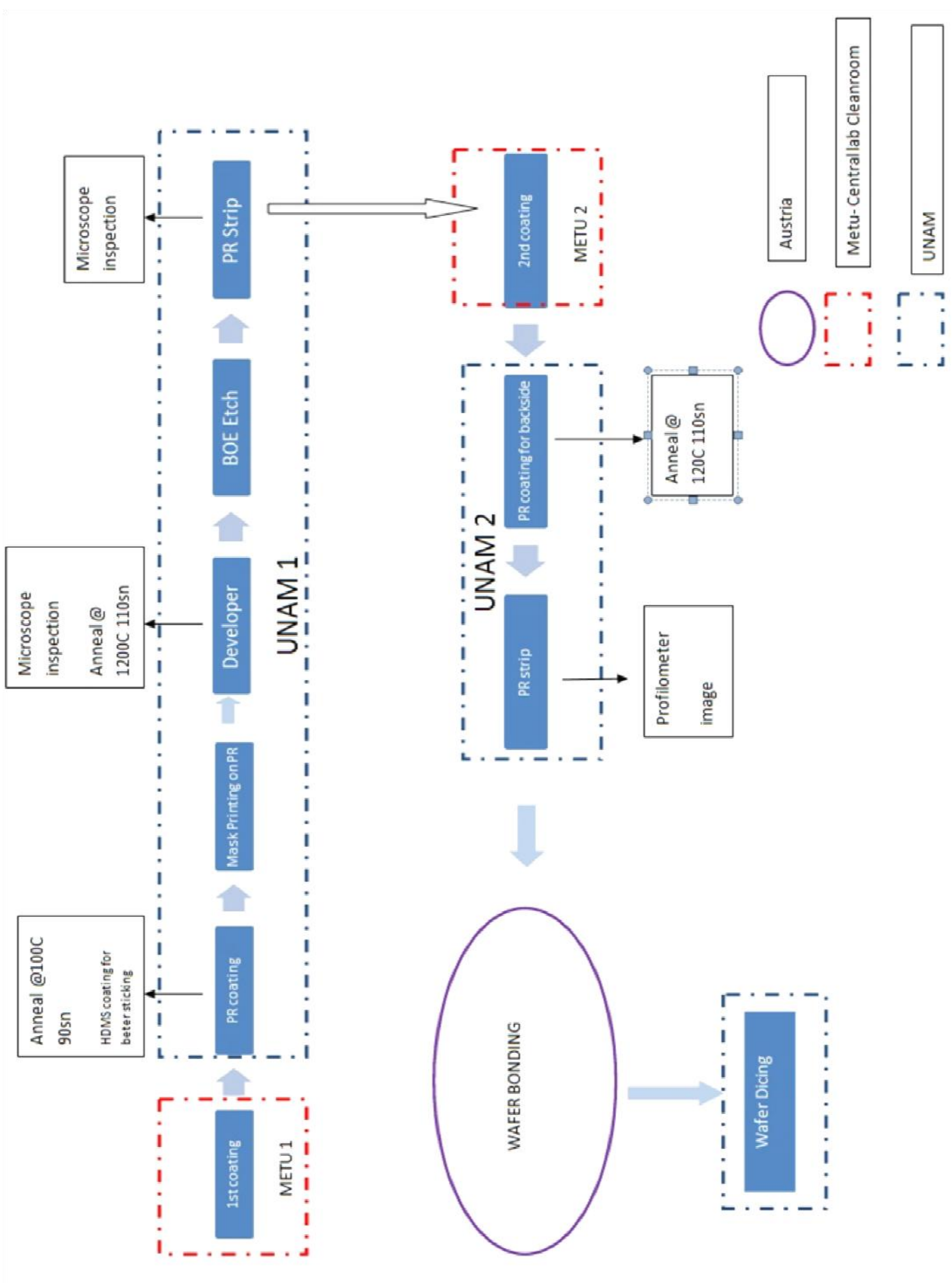

Figure 3.1 Fabrication process and facilities

3.1.1 OXIDATION OF SILICON WAFERS

The first step in the fabrication process is the oxidation of silicon wafers. All of the wafers are thermally oxidized to be coated silica layers. As discussed before material properties such as roughness, density of silica that is obtained by dry oxidation, well satisfy the requirements for further fabrication steps (wafer bonding). After controllable oxidizing and etching processes, and the bonding of wafer pairs, vacuum gap inside sample is obtained.

The gap heights (separation between plates) were formed using two dry oxidation steps with high precision. After the first oxidation photolithography and etching processes took place (step 2). Then the second oxidation was necessary to get silica layer as a radiative surface and to adjust the wall heights (Fig.3.2).

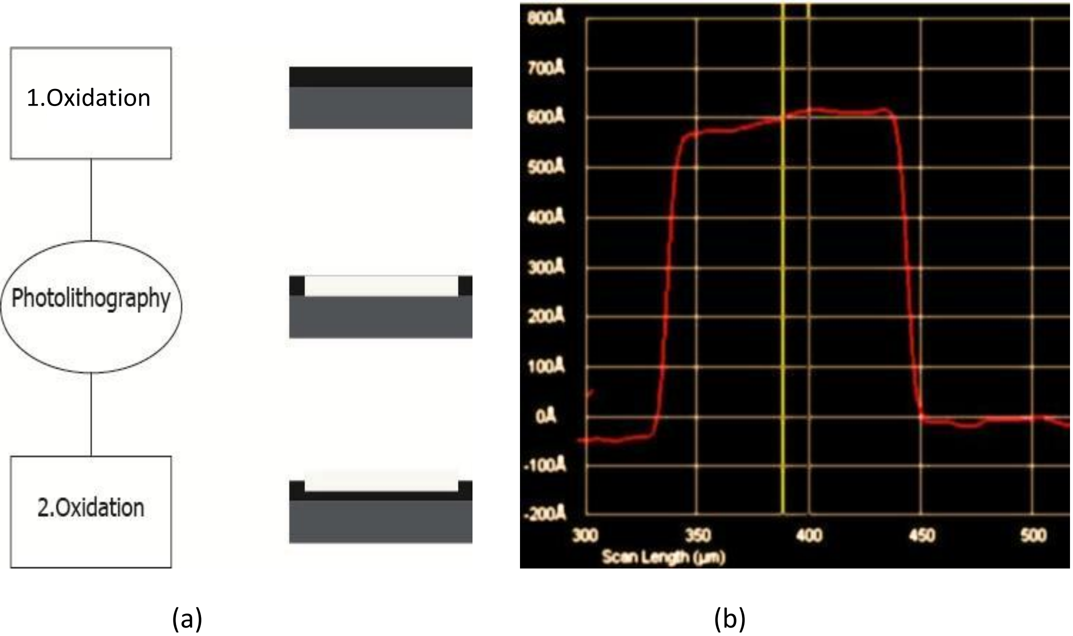

Figure.3.2 (a) First and second oxidation processes (b) Optical profilometer graph of a wall 50 nm gap height after the first oxidation.

To achieve better bonding and minimize the conduction heat transfer, the silica thicknesses are desired to be as high as possible. However, with the dry oxidation method it is time consuming process to achieve over 300 nm silica layer dry oxidation requires also pure oxygen which is expensive.

Oxidation

Basically oxidation is the interaction of oxygen molecules with the silicon wafer. According to the source of oxygen and environmental conditions, the oxidation processes can be classified as dry and wet oxidation. Thermal oxidation furnace in the cleanroom of Central Laboratory at METU, was used for dry and wet oxidation processes (Fig. 3.3).

Dry oxidation

The chemical reaction which describes dry process involves oxygen gas as the oxygen source:

$$Si_{(s)} + O_{2(g)} \text{ --> } SiO_2 \qquad (2.4)$$

During the dry oxidation the silicon wafer is placed in a pure oxygen gas atmosphere.

Wet Oxidation

Wet process uses steam as the oxygen source. The reaction for the wet oxidation:

$$2H_2O(g)+Si(s) \text{ --> } SiO_2+2H_2 \quad (2.5)$$

When thick oxides (>0.5 μm) are desired, generally steam is chosen as the source chosen.

Silicon wafers were placed in a quartz tube with quartz holder while the oxygen source flows over the wafers; see Figure 3.4 This procedure is performed at 1 atm pressure, and at the temperature 1100°C.

Fig. 3.3 Thermal oxidation furnace in METU-Central Laboratory Cleanrooms

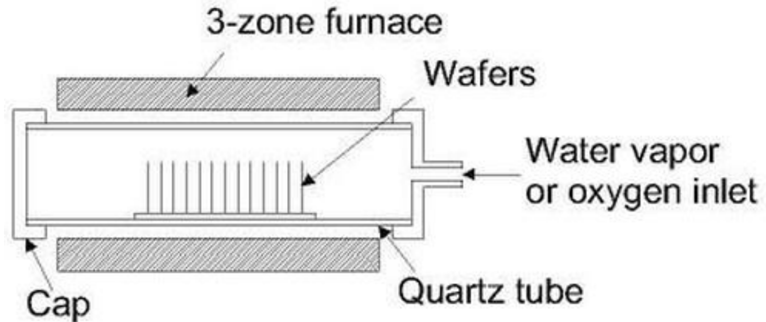

Fig.3.4 Schematic of quartz tube

The choice of oxidation technique depends on the thickness and oxide properties required. Compared with other oxides (wet, PECVD etc.) the dry oxide has better material characteristics and quality. Dry oxidation does not require the further annealing step for densification, and a smooth surface of roughness less than 1 nm may be obtained.

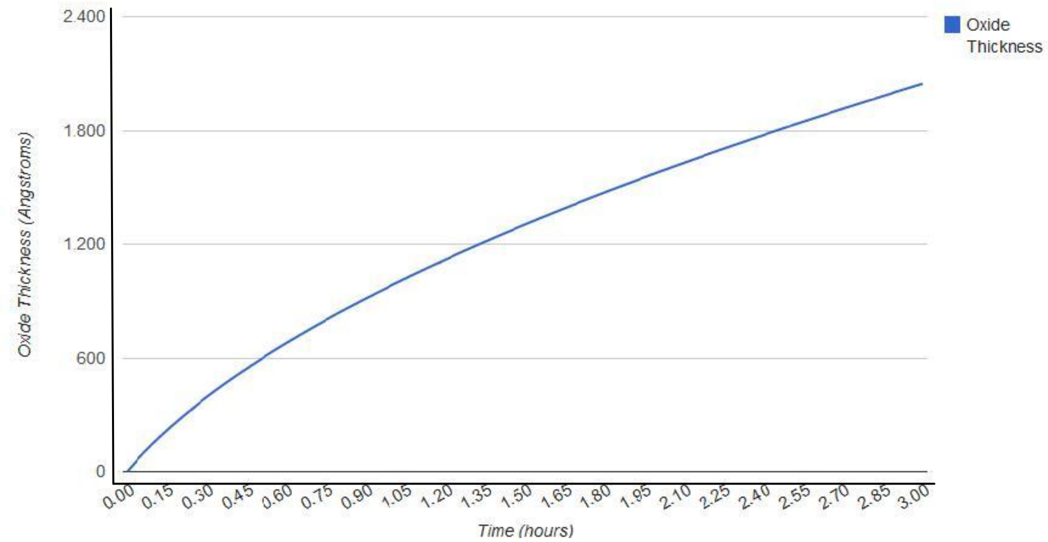

Fig. 3.5 Oxide thickness versus time graph for dry oxidation at 1100 °C

The rate of oxidation depends on the temperature. It is less than 100nm/hr at 1100°C operation temperature (Figure 3.5) [33]. Hence, the final oxide thickness can be controlled accurately. In the present work, the height of the gap has been controlled by controlling the wall height precisely with dry oxidation by using an online thickness calculator based on the Deal and Grove model. In this model, the transported oxygen in silicon wafer goes through the following stages:

(1) reacts or is absorbed by the outer surface of silicon;

(2) transported by diffusion across the oxide film towards the silicon;

(3) reacts at the silicon surface to form a new layer of $Si0_2$ (Fig. 3.6) [32].

Thermal oxidation is a well-known phenomenon and could be accurately modeled by an online calculator programme. An Online thickness calculator, prepared and published by Birmingham University was utilized for the required time corresponding to the desired thickness [33].

Oxidation simulation requires the wafer orientation (<111>/<100>) temperature, time, oxidation ambient wet/dry, and initial oxide thickness as inputs.

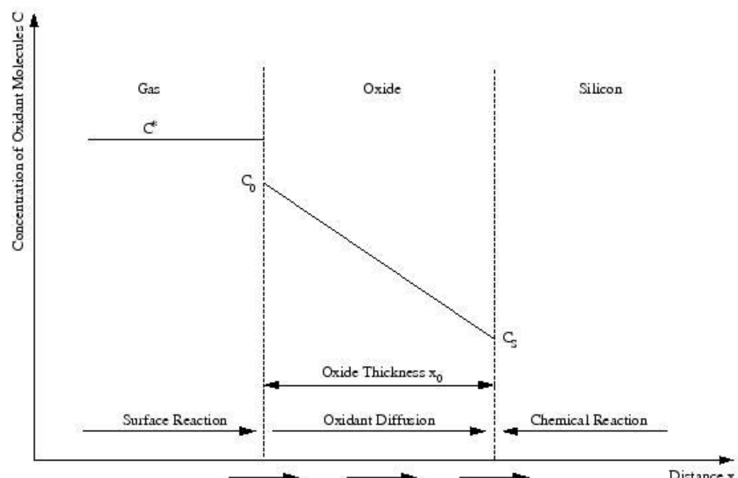

Figure 3.6 One dimensional model for oxidation of silicon [36]

An ultra pure oxygen source is utilized for dry oxidation to attain a defect free silica layer. Since ultra pure oxygen sources are quite expensive, it’s important to use the oxygen source economically. Therefore, the total silica thickness is arranged slightly more than thickness required for valid bonding.

An unexpected ring shaped silica layer has been formed on the wafer with wet oxidation. Ring shapes correspond to variations of silica layer thickness. Changing parameters such as gas flow rates, direction of wafers in quartz tube and operation temperature, could not eliminate the ring shapes.

3.1.2 LITHOGRAPHY

Lithography is one of the key steps in micro-fabrication, and can be basically defined as transferring desired patterns to the wafer. With lithography techniques, structures down to micrometer size can be fabricated. It is possible to print several structures on

the wafer at the same time. Once the original image is transferred to a mask, it is possible to transfer this image or patterns on to several wafers. Fabrication costs reduce due to the mass production opportunities in micro-fabrication.

Over one hundred samples of different size (1x1, 2x2, 5x5 and 19x19 mm^2) and different wall thickness (1.5µm, 2µm, 3µm) have been printed on wafer at the same time with lithography.

Photolithography technique was used rather than e-beam lithography which has much greater resolution for patterning. Features, smaller than 2 µm, can be fabricated with photolithography.

Choosing the wall thickness values has critical importance for the sample preparation. Walls must be as thin as possible to reduce the contribution of conduction heat transfer via walls. At the same time, walls must be of enough thickness for satisfying bonding requirement and having the capability of holding vacuum in the gap for a meaningful period of time. Walls with 2 µm thickness can be made with photolithography easily and faster than e-beam lithography. Bilkent UNAM cleanrooms have been used for this process. Below steps of photolithography process will be discussed.

3.1.2.1 MASK PREPARATION

Optical masks are designed and fabricated in order to print the desired structures on the photoresist coated wafers by selectively exposing them to UV light. Once the mask is prepared, the same pattern can be applied to several wafers, eight in our case. Over one hundred sample patterns have been printed on a glass plate with the etching of chromium (Cr).

Alignment marks have been placed as well as the sample patterns on the masks to align the matching structures on the wafers, and to determine the right coordinates for dicing after the wafer bonding process.

DWL 66 Heidelberg instrument was used as the mask writer at UNAM. L- edit pro software has been used for designing the patterns (Fig. 3.7).

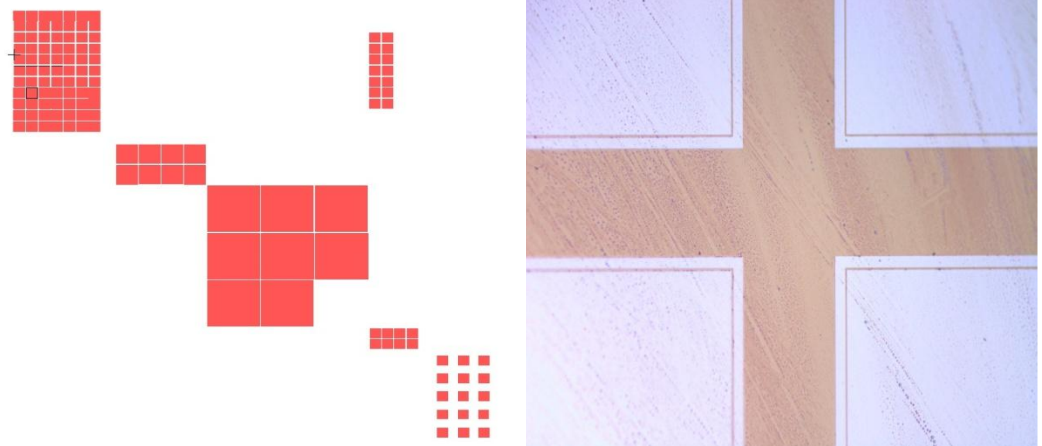

Fig 3.7 (a) Image of mask prepared with L-edit Pro software (b) patterns on wafer after etching image taken with optical microscope.

3.1.2.2 SURFACE PREPARATION

Microfabrication takes place under highly controlled conditions. All materials must be carefully selected. Water, gases and chemicals used in the fabrication process must be purified of contaminants (Dust, native oxide, residue of photoresist or solvents) on the silicon wafer surface must be removed prior to further steps. Surface preparation is not only the cleaning of the wafer, rather leaving the surface in a known and controlled condition.

3.1.2.3 PHOTORESIST COATING

Photoresist is a photosensitive material and exposure to UV light can change some of its chemical properties. Photoresist is used to transfer the pattern defined by the optical mask to the wafer.

Before the photoresist (PR) application, wafer is coated with adhesion promoter HMDS to make the wafer hydrophilic. This prevents the condensation of the moisture and improves the adhesion of the photoresist to the surface.

Exposure to UV light changes PR solubility which enables the selective removal of the resist in the development step. In positive PR, the exposed areas become more soluble in the developer, and in negative resist the exposed parts become insoluble. So with appropriate chemical selection it can be chosen if the parts exposed to light would removed or vice versa.

This resist pattern can be used as an etch mask. The photoresist must be chemically resistant to whichever etchants are to be used.

Photoresist is coated on the wafer surface with spin coater. Wafers are first fastened with vacuum chuck, then appropriate chemicals are added while the wafer is rotated at high speed. According to the type of the chemical and the rotation speed thickness of photoresist can be adjusted. 1.2-1.4 μm PMMA as the chemical has been coated at 1900 rpm in 40 seconds. After PR coating, the wafer is baked for 90 s at 100°C to evaporate the coating solvent and to densify the photoresist.

3.1.2.5 ALIGNMENT AND EXPOSURE

The pattern to be replicated on the wafer is first formed on the mask. When the mask is exposed to a UV light source, an image of the pattern is produced through the lens system. The image is then projected onto the photoresist coating of the silicon wafer using a projection system as illustrated in Figure 3.6 a.

3.1.2.6 DEVELOPMENT OF PHOTORESIST

The photoresist is chemically sensitive to light, hence, only the exposed regions are developed (by solvent AZ 400) away leaving behind the mask pattern on the substrate (Figure 3.6 b).The solubility of the exposed areas in positive photoresist increases by factor of about one thousand. Hence, the un-exposed areas are untouched while the exposed areas quickly washed away. [37]

3.1.2.7 HARDBAKE

After the development stage wafer is heated 110°C for 110 seconds to remove any remaining solvents from the photoresist, and to prepare for further steps by improving the adhesion to the surface.

3.1.2.8 ETCHING OF SAMPLES

Etching is a subtracting method in MEMS technology used to remove the selected areas on the silica coated surface of the wafer. In general, etching processes can be classified into two groups;

Wet etching: the material is dissolved when immersed in a chemical solution.

Dry etching: the material is sputtered or dissolved using reactive ions or a vapor phase etchant.

The choice of an etching process is largely a matter of finding a chemical or reactive species that selectively attacks the film one wants to remove, while leaving the other areas of the wafer undamaged. Selectivity of an etchant can be defined as the ratio of etch rates of the two materials.

The etchant is chosen according to the material used and type of the etching method (dry or wet and isotropic or anisotropic). *Buffered HF (BHF)* is a very selective etchant for silica that stops etching when reaches the *silicon* and does not *etch* further (Figure 3.8 c). Photoresist (PMMA) protects the silica underneath against the silica etchant so that the pattern could be printed by etching the silica film with BHF. With careful control of etchant concentration, the etch rate is highly reproducible.

The etch rate of silica depends on the type of and concentration of the chemical and the type of the oxidation. Etch rate for 7:1 BHF is 100 nm/min [38].

3.1.2.9 PHOTORESIST REMOVAL

Once the etching step has been completed the photoresist is stripped. Stripping is performed with a wet process by introducing an appropriate chemical (solvent AZ 100).

The last step for lithography is the photoresist removal. After the lithography process, wafers are thermally oxidized again and the gap heights of 25 nm, 50 nm 100 nm and 200 nm are formed.

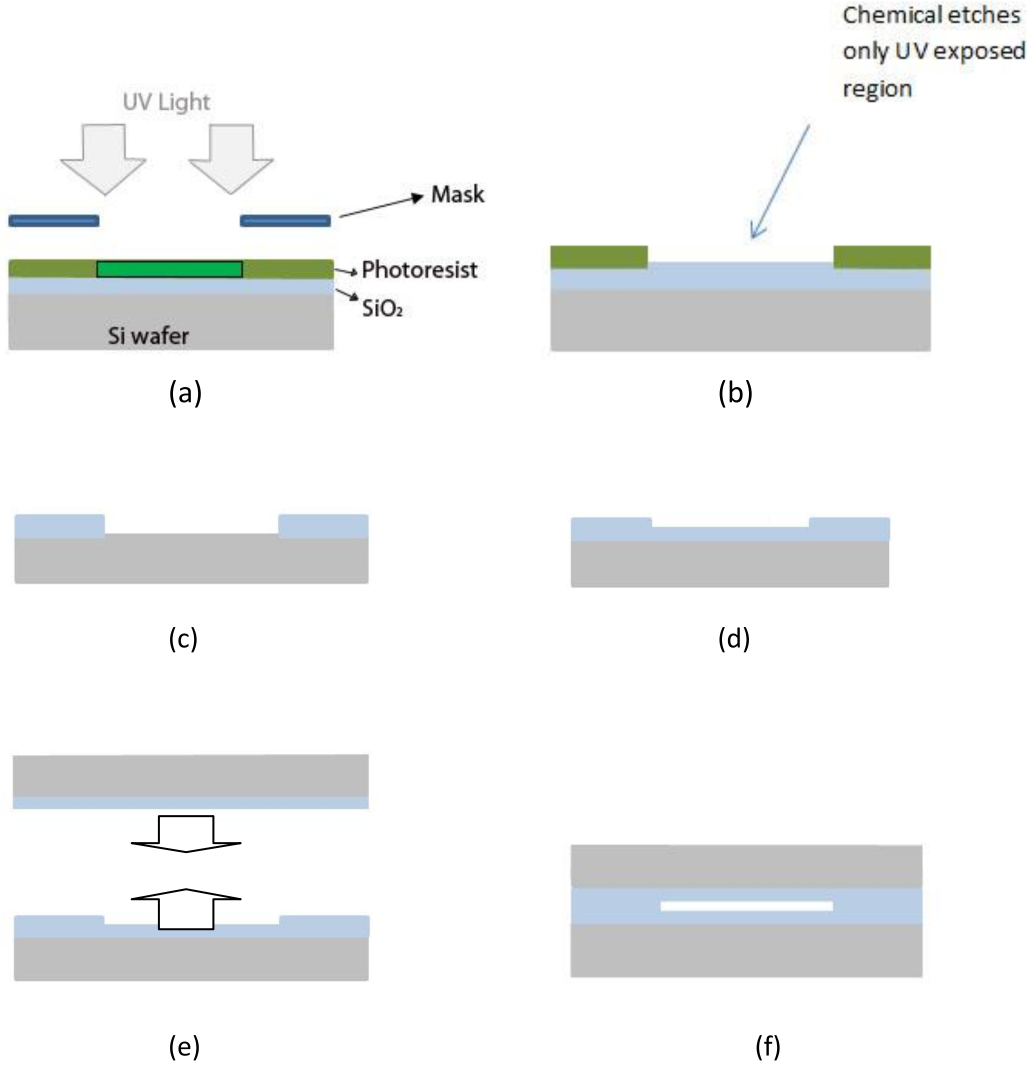

Figure 3.8 (a) Pattern replication on photoresist (b) photoresist removed with solvent (c) silica etched with chemical BOE (d) second oxidation process (e) bonding of patterned wafer and silica coated top wafer (f) sample after wafer dicing.

The structures have wall thicknesses of d = 1.2, 2, 3 and 5 μm. The walls of 1.2 μm and 1.5 μm thicknesses could be printed on the photoresist properly, however, were partially damaged after the etching. The bonding of 1.2 μm thick walls was not satisfactory either. The 2 μm, 3μm and 5 μm thick walls were well bonded to the top wafer (Figure 3.9).

3.1.3 WAFER BONDING

In the present study, the wafers were bonded to obtain vacuum gaps between them. Wafer bonding (WB) is a process used to join together two materials by bringing their surfaces into contact. Adhesion occurs between the two surfaces if certain requirements are fulfilled: surfaces have to be flat, smooth (typically of micro-roughness below 0.5 nm), and clean [39].

Wafer bonding became a key technology in various MEMS devices manufacturing. With wafer bonding 3-D structures can be formed. In order to obtain a vacuum gap between the two wafers this technique is utilized.

The touching surfaces of the wafers are coated with silica. Hence, the bonding takes place between two silica coated surfaces.

Plasma activated wafer bonding is a surface activation method in which a plasma treatment is applied to the wafers prior to bringing them into contact for bonding. The surface chemistry can be tailored in order to obtain maximum bond strength for low temperature thermal annealing.

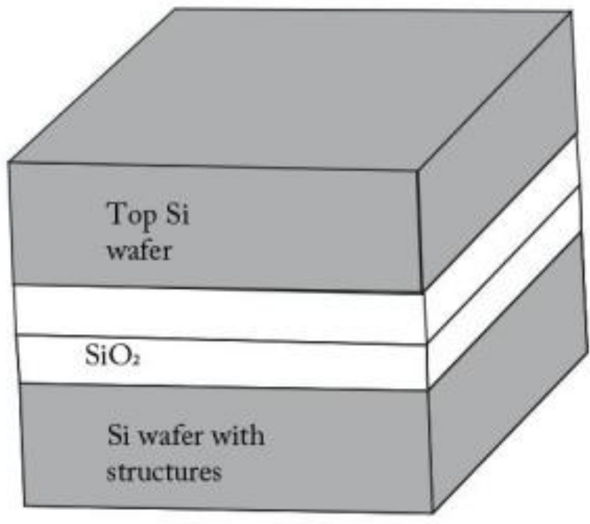

Fig 3.9 Bonded wafers with vacuum gap inside

Different wafer bonding approaches (direct, euctetic, thermo compression and anodic bonding) are currently used in MEMS manufacturing. The bonding method can be decided according to the type of surfaces that will be bonded. Fusion (direct) bonding (low temperature plasma activated wafer bonding) method has been utilized because with this method it is able to bond two silica surfaces. Bonding process took place under vacuum conditions (10^{-3} mbar chamber pressure) so that the vacuum inside the gap can be obtained.

The method is based on molecular bonds being established between molecules from the surfaces of the two substrates. In fusion bonding process, the wafers are exposed to plasma treatment prior to getting in contact for bonding.

Wafer bonding process flow consists of the following steps (Fig 3.10):

1. Plasma activation was performed using oxygen and nitrogen plasma activation system. Both wafers were activated. Oxygen or nitrogen plasma are used for activation.

Surface activation (O_2 or N_2 plasma treatment) consists of a wet or dry chemical treatment of the substrate surface which enables the formation of strong chemical bonds. This way, the thermal annealing temperature and its duration decreases. Wet chemical processes usually involve hazardous chemicals and some are not be applicable to the present case. Hence, a dry activation method (plasma) is utilized.

2. The wafers are cleaned using a megasonic cleaning nozzle.
3. Bonding alignment has been performed using the alignment marks.
4. Bonding is realized in EVG520 semi-automated bonder: The wafers are placed in the bonding chamber that was evacuated down to 10^{-3} mbar to avoid trapping of air at the interface. After bringing the wafers into contact, a 10,000 N force was applied for one hour at 300°C [40].

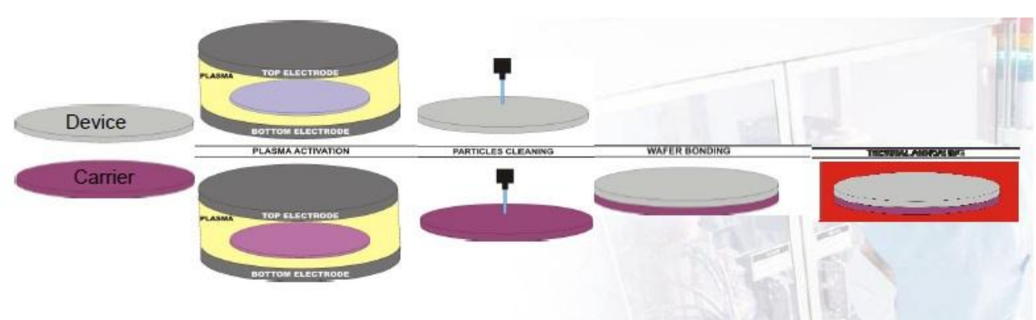

Fig 3.10 Fusion bonding steps.

A C-SAM (C mode Scanning Acoustic Microscope) image of a wafer pair is given in Figure 3.11.a The image is taken after the bonding for characterization. The samples are inspected for voids. The voids are mainly caused by particles, organic residues, surface defects, and inadequate mating. The dark areas in Figure 3.11.b show the well bonded parts while the white regions indicate poor bonding [41]. Some voids

may be observed from the figure. The 1 x 1, 2 x 2, 5 x 5, and 20 x 20 mm² structures may be seen as white due to the gap inside.

The middle portions of the 5 x 5 and 20 x 20 mm samples are seen as black. The reason is believed to be the deflection and touching of the top and bottom wafers due to the difference between the pressure inside the gap and the atmospheric pressure.

Testing the bonding quality:

Sonoscan D9000 instrument was used for the inspection of the bonding quality and voids.

The C-SAM®, or C-Mode Scanning Acoustic Microscope, is a very high frequency such as 230MHz or 300MHz pulse-echo ultrasonic microscope that generates images by mechanically scanning a transducer over a sample [42].

The ultrasonic transducer that scans the wafer pair pulses UHF ultrasound onto the top surface and receives the return echoes. Transmitted or reflected waves are collected if acoustic impedance (due to elastic properties of materials) mismatch between silicon and air bubbles that will result in a large amount of scattering.

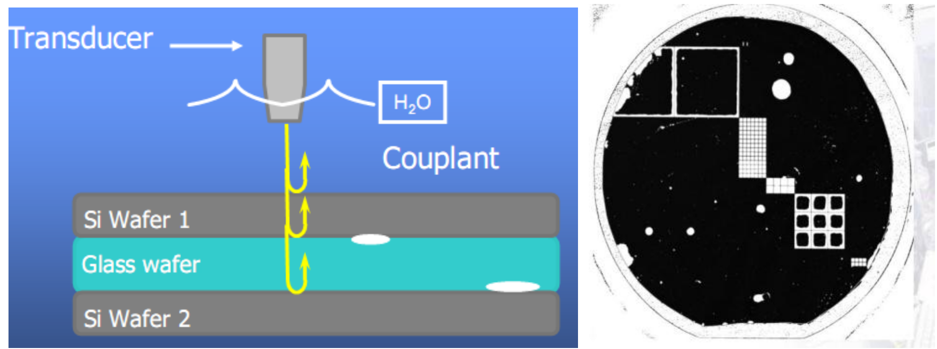

Fig. 3.11 (a) C-SAM [42] (b) C-SAM micrograph

This provides a basis for investigating anomalies at specific depth levels. Voids, cracks, unbounded areas and delaminations provide high contrast and are easily distinguished.

3.1.4 WAFER DICING

After the wafer bonding the last step for sample preparation was cutting of the wafers to get individual samples which can be later mounted into the test equipment. Two facilities and two different instruments have been used for this process.

Disco dicing saw model DAD341 at UNAM has been utilized for wafer dicing. Dicing machine has 200 µm and 60 µm diamond knives. During the dicing, the knives turn at 1900 rpm and a chuck holding wafer moves along the cutting line with pressured water for cooling during the dicing. Since 60 µm thick knives, were not sufficiently strong to dice the bonded wafers and broken easily after one or two dicing line, 200 µm thick knives have been used.

Dicing saw is fast and can be programmed which enables serial cuttings but especially high aspect-ratio topography and other pressure-sensitive components may not withstand the impact of the pressured water for cooling encountered during the dicing and dicer knife pressure.

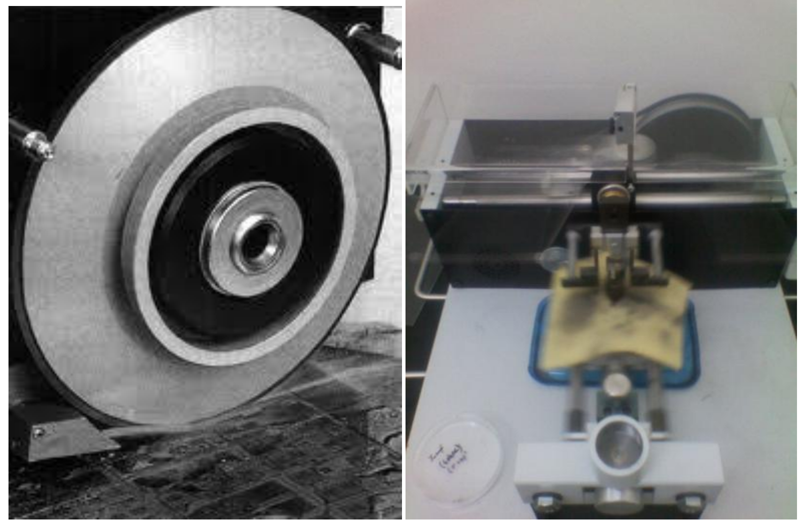

Fig. 3.12 (a) Wafer dicer's blade (b) wire cutter

The well bonded (according to C-Sam image) samples with 100 nm and 200 nm gaps could be diced but relatively weaker bonded pairs with 25 nm and 50 nm were broken from the thin silica wall connections.

A wire cutter for dicing wafer pairs has been employed in order to overcome the challenges. The wire cutter exerts a very low pressure on the wafer by 60 µm wire and it is very slow compared to the dicing saw machine. Wire cutter is located at GÜNAM laboratories in METU Physics Department.

Due to the disorientation of patterns during the wafer bonding process, determining the correct line for dicing was difficult. By determining the shifting amount at vertical and horizontal directions by the inspection of diced sample under SEM or optical microscope, dicing from the correct line to get better individual samples has been achieved (Figure 3.13).

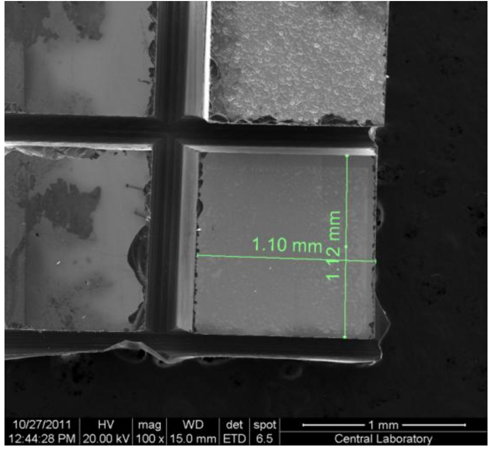

Fig. 3.13 SEM micrograph of a diced sample.

3.2 DISCUSSIONS ON FABRICATED SAMPLES

The quality of samples has been varied. Some samples could not be used because silica plates were not bonded well and they swept away during the wafer dicing process due to pressured water, which was used to cool the dicer blade. Some samples (5x5 and 19x19 mm²) could not be used as they had collapsed surfaces each

other because of the pressure exerted during the wafer bonding. The micrographs of the gap between wafers obtained by Scanning Electron Microscope (SEM) are shown in Figure 3.14.

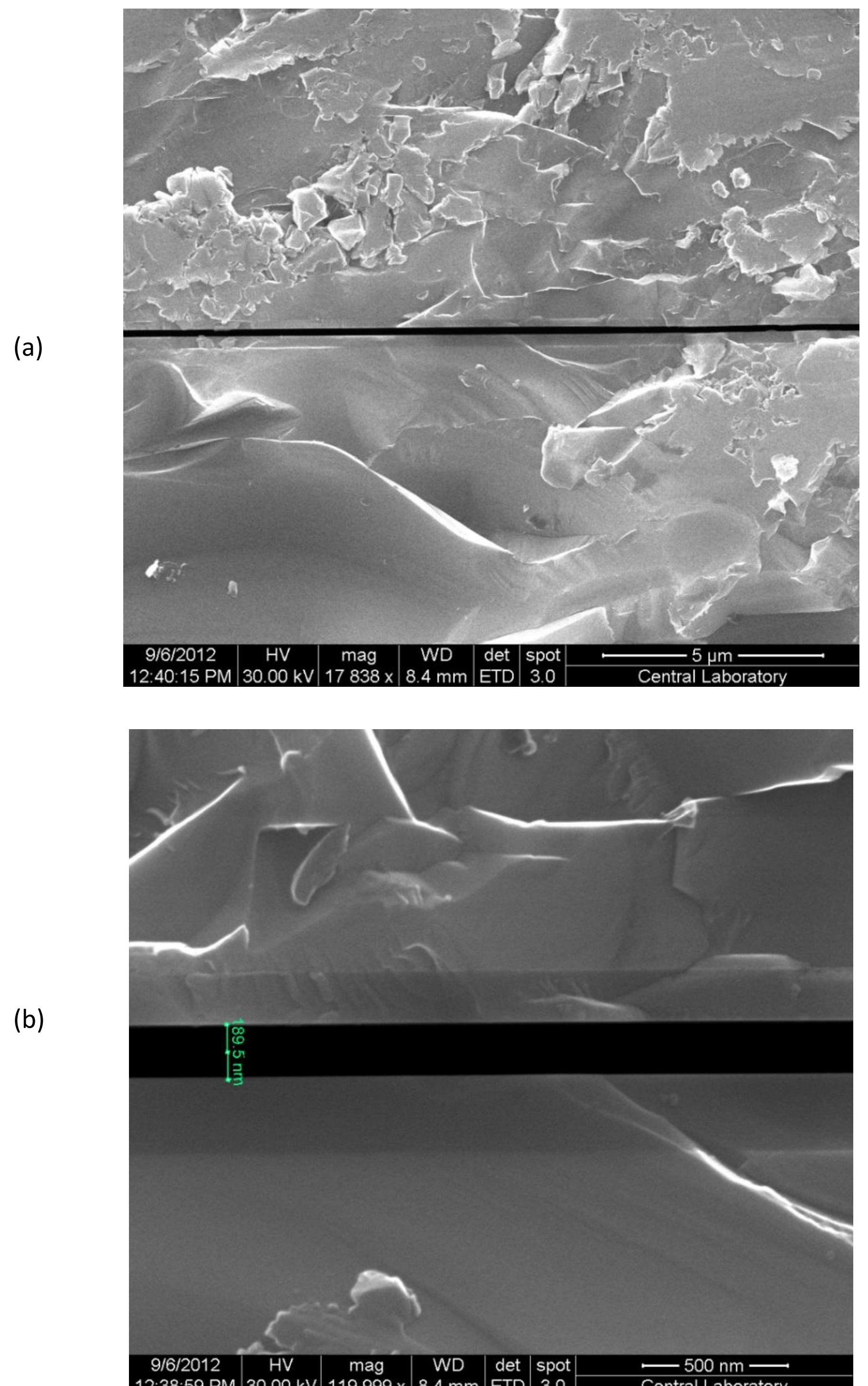

Figure 3.14 SEM Separation between silica coated silicon wafer at at magnification (a) 18000X and (b) 120000X.

One of the biggest problems was the alignment failure of the wafers during the wafer bonding. Since the top wafer had no pattern on it, the problem was occurring during dicing the samples individually from the wafer.

The alignment error was about 200 μm horizontally and 50 μm in the vertical direction. The values slightly changed for different pairs.

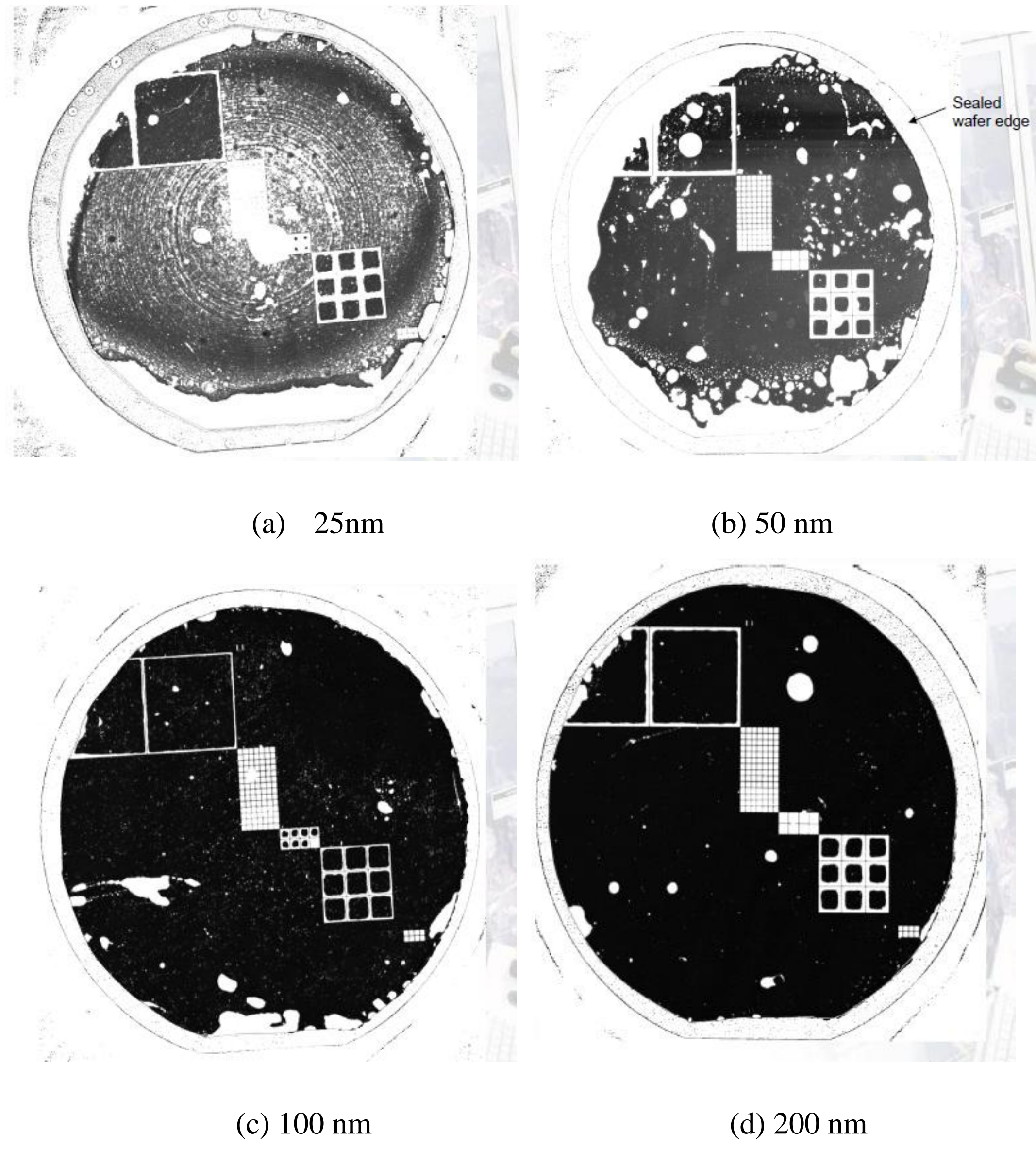

(a) 25nm (b) 50 nm

(c) 100 nm (d) 200 nm

Fig. 3.15 Bonding qualities by inspection with C-SAM microscope.

According to C-SAM images it can be seen that the quality of the bonds which was

achieved with oxygen plasma is better than the bonds made with nitrogen plasma. The first two bonds were made with nitrogen plasma (including 25 and 50 nm gaps) and the others were bonded with using oxygen plasma (100 nm and 200 nm) (Fig. 3.15).

3.3 TEST SETUP

The investigation of near field radiation transfer has been conducted by two study groups: sample design and fabrication were done by the group in Ankara, test setup construction and the tests by the group in İstanbul. This setup was designed and established by D. Kurt Webb at Özyeğin University laboratories.

The experimental setup is designed to heat the sample, remove heat from the sample at steady state and monitor a sample's plate temperatures and incident heat flux. The total heat flux, which consists of conduction through silica walls and near field radiative heat flux, was measured at steady state (Fig. 3.16). Since our samples were fabricated to hold vacuum inside, in contrast with previous experimental tests, it was able perform tests at atmospheric pressure.

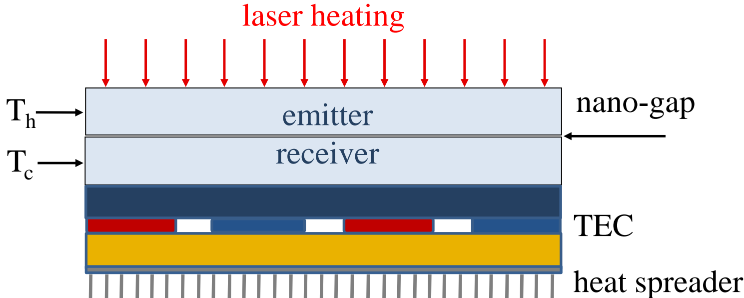

Figure 3.16 Testing sample

In general the test setup consists of the following parts: a heat source (laser), heat sink (sample cooler), beam splitter, thermo-couples. A generic setup, including a laser heat source focused on a sample using an optical train, power meter flux

measurement system, data acquisition unit and their relation to the test sample, are shown in Fig. 3.17.

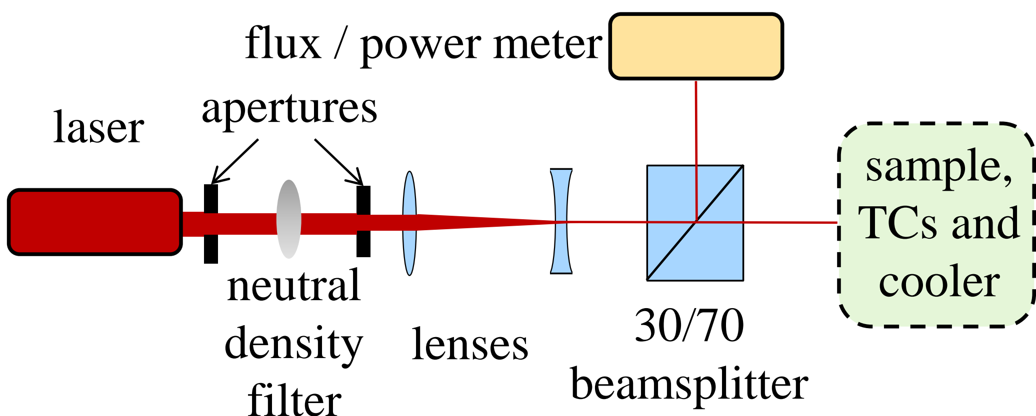

Figure 3.17 Test setup at Özyeğin University

Thermocouples were used for temperature measurements by placing temperature probes' tips on the emitter (heated by laser sorce) and receiver (attached to TEC) side of the wafer sandwich. A 660 – 680 nm (red), 190 mW laser is used as the heat source focused on the sample. The portion of the total laser light passing through was controlled from 100% to 0% or 190 mW to 0 mW by using a density filter.

The beam then passes through a 30/70 beam splitter, which reflects 30% of the beam to an optical power meter. 70% of the beam is transmitted through the beam splitter and is incident upon the sample.

To provide steady state cooling of the sample to balance the incoming flux from the laser heat source, a Nextreme UPF4 Optocooler^{TM} thermoelectric cooler (TEC), heat sink was used as shown in Fig. 3.18.

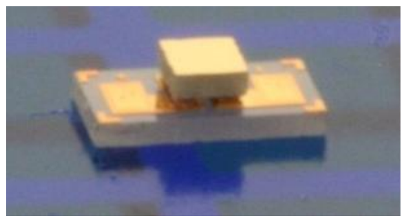

Figure 3.18 Nextreme UPF4 Optocooler TM thermoelectric cooler. (1.5x2.5 mm^2 footprint).

The cold side is 0.74x0.74mm^2 which is well fitted to our 1x1 mm^2 samples. The entire surface of the cooler attached to the sample, so all the heat drawn through that surface will be coming from the sample.

Tests for 100 nm and 200 nm gap height samples were done and results will be discussed in next section. However, 25 nm and 50 nm samples could not be investigated as the laser source went out of order.

3. 5 PRELIMINARY TEST RESULTS

The measurement results have been plotted against the predicted total heat transfer by D.Kurt Webb in his thesis study [44]. Predicted values denoted as Q_{vac} are for total heat transfer for the sample that holds vacuum inside. Q_{air} stands also for total heat transfer through samples with air inside the gap. The sum of the near field and far field radiative heat transfer was also plotted, and denoted as Q_{rad}.

Q_{rad}, Q_{vac} and Q_{air} were calculated at multiple temperature difference values and plotted. These along with data points from the experiments are shown in Figure 3.19 for the 100 nm gap sample and in Figure 3.20 for the 200 nm gap sample.

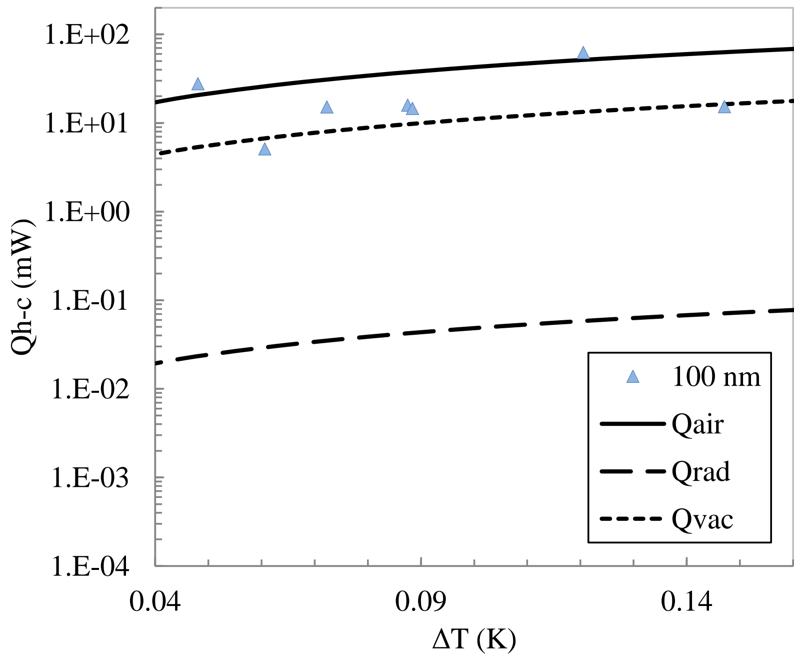

Figure 3.19 Total heat transfer rate vs. difference in measured temperatures (d=100nm) [44].

The results of the tests performed with a 100 nm gap sample show a correlation with Q_{vac} as well as Q_{air} The data also correlate the combination of conduction through air, walls and radiation (Q_{air}). .

There were too many uncertainties from samples and measurement setup such as thermocouple accuracy, thermocouple positioning, positioning of flux measurement. All contributed to the final uncertainty in the predicted radiative transfer between plates (Appendix A).

All values used throughout the project were taken as averages of 60 values. To achieve steady state heat flux, long measurements were taken and the 60 consecutive values of the most stable data were manually selected. Experimental results are tabulated in Appendix B.

In summary, methods were developed to obtain a measurement of heat flux between plane-parallel plates. The total flux between plates correlates with either the vacuum, Q_{vac}, or non-vacuum, Q_{air} calculations, but there is too much experimental

uncertainty to verify whether either of these is the case.

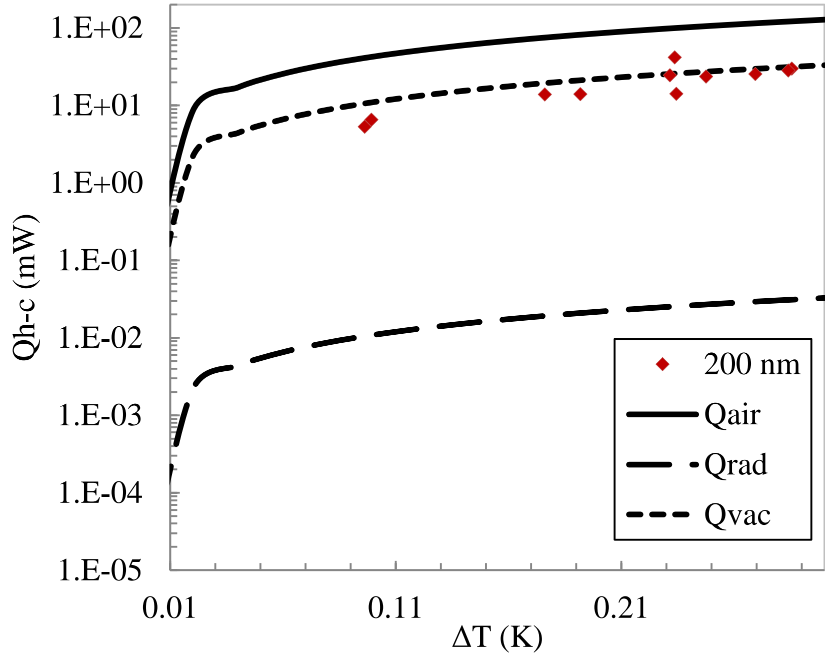

Figure 3.20 Total heat transfer rate vs. difference in measured temperatures (d=200 nm) [44].

CHAPTER 4

CONCLUSIONS

4.1 DISCUSSION AND CONCLUSIONS

An appropriate method for the fabrication of nanostructured 3D samples by using MEMS fabrication methods have been developed and realized have been realized by this study. Nanometer sized gaps between two parallel planes have been obtained. Only small fraction of fabricated samples has been tested, and measurement results showed enhancement in near field radiation heat transfer.

Silica coated silicon wafer sandwiches have been fabricated to investigate the heat flux enhancement between nanometer spaced surfaces. Although near field effects have been discussed for many years, experimental verification of these effects is very limited. MEMS fabrication methods (oxidation, lithography and wafer bonding) have been used to prepare a variety of samples with 1x1, 2x2, 5x5 and 19x19 area and with 25 nm, 50 nm, 100 nm and 200 nm separations. 3-D structures have been obtained by bonding of the wafers. Four facilities have been utilized for the whole fabrication process: 1- METU Central Laboratory Cleanrooms for thermal oxidation. 2-BİLKENT UNAM Cleanrooms for photolithography 3- EVG Company for wafer bonding in Austria, 4-GÜNAM laboratories for wire cutter equipment.

As we designed the samples with dimensions at around the limitations of the used instrument, deviations from the expectations occurred for each fabrication process at

different levels. Patterns have been printed on the silicon wafer accurately except those with 1.2 µm thick walls because of the limits of optical lithography. Samples which have over 1.5 µm wall thicknesses could be deposited regularly. Samples with dimensions 5x5 mm^2 and 19x19 mm^2 collapsed during the wafer bonding process due to high pressure applied.

Wafer bonding quality was not sufficient for samples that were bonded by means of nitrogen plasma. Utilizing oxygen plasma resulted in better bonding quality.

Another major challenge in fabrication has been faced during the dicing of the bonded wafers. This was due to the misalignment of the wafers during the wafer bonding process. The high pressure induced by the cooling water of the wafer dicer at UNAM also introduced some damage to the delicate samples.

In addition, many experimental uncertainties have been reported by the joint study group members.

Despite the challenges discussed, over one hundred samples have been fabricated and successfully bonded; the diced samples could be tested with the experimental setup at Özyeğin University. An increase in the net radiation heat transfer with decreasing nano-gap size has been reported by the Özyegin group which used these samples in a parallel study.

4.2 FUTURE WORK

In this study, test samples have been fabricated for investigating the enhancement of heat flux in the near field. Samples with higher surface area to wall thicknesses ratio improve the contribution of the near field heat transfer rate over other transfer modes. Therefore, rather than decreasing the wall thicknesses, samples with higher surface areas than 1x1 mm^2 should be successfully fabricated.

Wafer bonding quality has to be improved in order to obtain better results. The test result showed questionable vacuum level inside the gap for samples with 100 nm

separation. Thus, samples should be tested for the vacuum level inside the gap by an appropriate measurement system.

Uncertainties regarding the sample and measurement setup must be lowered by using more sensitive testing equipments.

Samples that contain heat source and thermocouples attached by using appropriate MEMS fabrication methods can be designed to minimize the positioning errors.

REFERENCES

[1] Richard P. Feynman California Institute of Technology, Engineering and Science magazine, vol. XXIII, no. 5, February 1960

[2] www.nano.gov last visited 12.08.2012

[3] M. Planck, “The theory of heat radiation”, (Dover, New York, 1959).

[4] M. Francoeur, "Near-field radiative transfer: thermal radiation, thermophotovoltaic power generatıon and optıcal characterization", Doctoral Dissertations. Paper 58. (2010)

[5] S. Basu and Z. M. Zhang, “Maximum energy transfer in near-field thermal radiation at nanometer distances”, Journal of Applied Physics 105, 093535 (2009)

[6] K. Joulain, J. Mulet, F. Marquier, R. Carminati, J.Greffet “Surface Electromagnetic Waves Thermally Excited: Radiative Heat Transfer, Coherence Properties and Casimir Forces Revisited in the Near Field” Elsevier Science (2008)

[7] N.N. Lal, A.W. Blakers. “Silver cells in thermophotovoltaic systems”, Solar Energy Materials & Solar Cells 93 (2009) 167–175

[8] M. Laroche, R. Carminati and J.J. Greffet. “Near-field thermophotovoltaic energy conversion”, Journal of Applied Physics 100, 063704 (2006)

[9] S.M.Rytov, Y.A.Kravstov and V.I.Tatarskii, “Principles of Statistical Radiophysics”, Springer-Verlag, Berlin,1989.

[10] D.Polder and M.VanHove. "Theory of radiative heat transfer between closely spaced bodies", Phys.Rev.B 4,3303 (1971)

[11] C.M.Hargreaves, “Radiative transfer between closely spaced bodies”, Phys.Lett.A 30,491 (1969).

[12] M. Francoeur and M. P. Mengüç, “Role of Fluctuational Electrodynamics in Near-Field Radiative Heat Transfer,” Journal of Quantitative Spectroscopy and Radiative Transfer, 109 (2008) 280-293

[13] M. Francoeur, M.P. Mengüç and R. Vaillon ”Local density of electromagnetic states within a nanometric gap formed between two thin films supporting surface phonon-polaritons,” J. Appl. Phys., in press, 2010.

[14] M. Francoeur, M.P. Mengüç, and R. Vaillon, "Coexistence of multiple regimes for near-field thermal radiation between two layers supporting surface phonon-polaritons in the infrared," Physical Review B 84, 075436, 2011

[15] M. Francoeur, R. Vaillon, and M.P. Mengüç, "Thermal impacts on the performance of nanoscale-gap thermophotovoltaic energy conversion devices," IEEE Transactions on Energy Conversion, 26(2), 686-698, 2011

[16] M. Francoeur, M.P. Mengüç, and R. Vaillon, "Control of near-field radiative heat transfer via surface phonon-polariton coupling in thin films," Applied Physics A: Materials Science & Processing, 103(3), 547-550, 2011

[17] M. Francoeur, M.P. Mengüç, and R. Vaillon, "Solution of near-field thermal radiation in one-dimensional layered media using dyadic Green's functions and the scattering matrix method," Journal of Quantitative Spectroscopy and Radiative Transfer 110, 2002-2018, 2009

[18] M. Francoeur, M.P. Mengüç, and R. Vaillon, "Spectral tuning of near-field radiative heat flux between two thin silicon carbide films," Journal of Physics D: Applied Physics 43, 075501, 2010

[19] M. Francoeur, M.P. Mengüç, and R. Vaillon, "Near-field radiative heat transfer enhancement via surface phonon polaritons coupling in thin films," Applied Physics Letters 93, 043109, 2008

[20] C. M Hargreaves "Radiative Transfer between Closely Spaced Bodies," Philips Research Reports and Supplement" Philips Research Reports and Supplement, Vol. 5, pp. 1-80 (1973)

[21] G.A.Domoto, R.F.Boehm and C.L.Tien, J.Heat Transfer 92,412(1970).

[22] A. Narayanaswamy, S.Shen, and L.Hu, Appl. Phys. A 96,357 (2009).

[23] R. Ottens, V. Quetschke, S. Wise, A.A. Alemi, R. Lundock, G.Mueller, D.H.Reitze, D.B.Tanner and B.F.Whiting 1103.2389v1 Physics Optics 2011

[24] Xu, J. B., K. Läuger, R. Möller, K. Dransfeld, and I.H. Wilson, "Heat transfer between two metallic surfaces at small distances", J. of Appl. Phys., Vol. 76, No. 11, pp. 7209-7216 (1994)

[25] A. Kittel, W. Muller-Hirsch, J.Parisi, S.A.Biehs, D. Reddig and M. Holthaus, Phys. Rev. Lett. 95,224301 (2005)

[26] S. Shen, A. Narayanaswamy and G.Chen, Nano Lett. 9, 2909 (2009).

[27] V. S. Arpacı, A. Selamet and Kao, S.H. "Introduction to Heat Transfer. Upper Saddle River" Prentice Hall. (2000)

[28] L. Hu, A. Narayanaswamy, X. Chen and G. Chen. "Near-field thermal radiation between two closely spaced glass plates exceeding Planck's blackbody radiation law." Applied Physics Letters 92, 133106 (2008)

[29] Timoshenko, S., and S. Woinowsky-Krieger, "Theory of plates and shells.", McGraw-Hill Inc. (1959)

[30] M.A. Hopcroft, W. D. Nix and T. W. Kenny, "What is the Young's modulus of silicon?", Journal of Microelectromechanical Systems, 229-238. (2010)

[31] H. Greenhouse, "Hermeticity of Electronic Packages" 2nd Edition 2011 Elsevier Books.

[32] B.E. Deal and A. S. Grove, "General Relationship for the Thermal Oxidation of Silicon,", J. Appl. Phys., 36, 3770 (1965)

[33] http://www.cleanroom.byu.edu/OxideThickCalc.phtml last visited 12.08.2012

[34] American Vacuum Society J. Vac. Sci. Technol., 10,p 543, W.G Perkins copyright (1973)

[35] Z.M. Zhang "Nano/Microscale Heat Transfer", McGraw Hill Nanoscience and Technology Series. p.122 (2007)

[36] http://www.iue.tuwien.ac.at/phd/hollauer/node16.html# SECTION0066100 last visited 15.08.2012

[37] T.Fukuda, W.Menz "Micro Mechanical Systems: Principles and Technology */Handbook of Sensors and Actuators*", Elsevier Books (1998)

[38] Kirt R. Williams, Richard S. Muller. "Etch Rates for Micromachining Processing" Journal of Microelectromechanical Systems, vol. 5, no. 4, december (1996)

[39] V. Dragoi, S. Farrens "Plasma activated wafer bonding for MEMS" Proc. SPIE 5836, 179 (2005); doi:10.1117/12.608788

[40] A. Garnier, M. Angermayer, L. Di Cioccio, P. Gueguen and T. Wagenleitner, "Results on Aligned SiO2/SiO2 Direct Wafer-to-Wafer Low Temperature Bonding for 3D Integration" 978-1-4244-5232-3/09, 2009 IEEE.

[41] C Harendt, H G Graf, B Hofflinger and E Penteker, "Silicon fusion bonding and its characterization", 1992 *J. Micromech. Microeng.* **2** 113 doi:10.1088/0960-1317/2/3/001

[42] T. Adams Sonoscan Inc. "Looking acoustically into MEMS devices."
http://www.eetasia.com/statıc/pdf/201006/eeol2010jun09dtctrldta01.pdf?sources=download. Last visited 24.08.2012

[43] J.L. de Degovia "Physics of Outgassing"
http://www.cientificosaficionados.com/libros /cern/vacio9-cern.pdf Last visited 24.08.2012

[44] K. D.Webb "Measurement Of Near-Field Heat Transfer Between Plane-Parallel Silica Thin-Films" M.Sc. Thesis Boğaziçi University (2012)

[45] S. J. Kline and F. A. McClintock: "Describing Uncertainties in Single-Sample Experiments", Mech. Eng., p. 3, January 1953

APPENDICES

APPENDIX A: EXPERIMENTAL UNCERTAINTY CALCULATIONS

The experimental uncertainty calculations have been done by D. Kurt Webb [44]. To find the uncertainty interval of R, the second-power-equation is used which predicts the result's uncertainty value within ± 10% of the correct value [45]. The second-power-equation for any result r with uncertainty interval ω_r which is dependent on $v_1, v_2, \ldots, v_n$ with respective uncertainty intervals $\omega_1, \omega_2, \ldots, \omega_n$ is:

$$\omega_r = \left[\left(\frac{\partial r}{\partial v_1} \omega_1 \right)^2 + \left(\frac{\partial r}{\partial v_2} \omega_2 \right)^2 + \cdots + \left(\frac{\partial r}{\partial v_n} \omega_n \right)^2 \right]^{\frac{1}{2}} . \qquad \textbf{(A.1)}$$

Equation (A.1) is applied to all calculated values in all experiments. Applying the second-power-equation to find ω_R, the uncertainty interval of R, the equation is as follows.

$$\omega_R = \left[\left(\frac{\omega_{Qmeas}}{Q_{meas}} \right)^2 + \left(\frac{Q_{meas}}{Q_i^2} \omega_{Qi} \right)^2 \right]^{\frac{1}{2}} \qquad \textbf{(A.2)}$$

where ω_{Qmeas} and ω_{Qi} are the uncertainty intervals of Q_{meas} and Q_i respectively.

$$\omega_{Qi} = \left[\left(R\omega_{Qmeas} \right)^2 + \left(Q_{meas}\omega_R \right)^2 \right]^{\frac{1}{2}} \tag{A.3}$$

The uncertainty of the measured sample absorptivity is calculated in Equation A.4.

$$\omega_\alpha = \left[\left(\frac{\omega_{Qout,cond}}{Q_i} \right)^2 + \left(\frac{\omega_{Qconv}}{Q_i} \right)^2 + \left(\frac{\omega_{Qrad}}{Q_i} \right)^2 + \left(\frac{\alpha\omega_{Qi}}{Q_i} \right)^2 \right]^{\frac{1}{2}} \tag{A.4}$$

$$Q_{out,cond} = -k_{C11000} A_{Rod} \frac{\Delta T_{Rod}}{\Delta x} \tag{A.5}$$

By applying the second power equation to Equation A.5 for $Q_{out,cond}$, $\omega_{Qout,cond}$ is found to be

$$\omega_{Qout,cond} = \left[\begin{array}{l} \left(\frac{Q_{out,cond}}{k_{C11000}} \omega_{kc11000} \right)^2 + \left(\frac{Q_{out,cond}}{A_{Rod}} \omega_{ARod} \right)^2 + \\ + \left(\frac{Q_{out,cond}}{\Delta T_{Rod}} \omega_{\Delta TRod} \right)^2 + \left(\frac{Q_{out,cond}}{\Delta x} \omega_{\Delta x} \right)^2 \end{array} \right]^{\frac{1}{2}} \tag{A.6}$$

The second term in Equation A.4 is defined as

$$\omega_{Qconv} = \left[\left(\omega_{Qh,conv} \right)^2 + \left(\omega_{Qc,conv} \right)^2 \right]^{\frac{1}{2}} \tag{A.7}$$

where,

$$\omega_{Qh,conv} = \left[\left(\Delta T_h \omega_{hhAh} \right)^2 + \left(h_h A_h \omega_{\Delta Th} \right)^2 \right]^{\frac{1}{2}} \tag{A.8}$$

and

$$\omega_{Qc,conv} = \left[\left(\Delta T_C \omega_{hcAc} \right)^2 + \left(h_c A_c \omega_{\Delta Tc} \right)^2 \right]^{\frac{1}{2}} \tag{A.9}$$

The uncertainties of $h_h A_h$ and $h_c A_c$ are calculated in Equations A.9 and A.10 as;

$$\omega_{hhAh} = \begin{bmatrix} \left(\left(lh_v + th_{h,u} + th_{h,d} \right) \omega_w \right)^2 + \left(\left(2lh_v + wh_{h,u} + wh_{h,d} \right) \omega_t \right)^2 + \\ + \left(\left(\left(w + 2t \right) h_v \right) \omega_l \right)^2 + \left(\left(w + 2t \right) l \omega_{hv} \right)^2 + \left(wt \omega_{hh,u} \right)^2 + \left(wt \omega_{hh,d} \right)^2 \end{bmatrix}^{\frac{1}{2}} \tag{A.10}$$

$$\omega_{hcAc} = \begin{bmatrix} \left(\left(th_{h,u} + th_{h,d} \right) \omega_w \right)^2 + \left(\left(2lh_v + wh_{h,u} + wh_{h,d} \right) \omega_t \right)^2 + \\ + \left(2th_v \omega_l \right)^2 + \left(2tl \omega_{hv} \right)^2 + \left(wt \omega_{hh,u} \right)^2 + \left(wt \omega_{hh,d} \right)^2 \end{bmatrix}^{\frac{1}{2}} \tag{A.11}$$

The uncertainties in h_v, $h_{h,u}$, $h_{h,d}$, the respective free convective vertical, horizontal up-facing, and horizontal down-facing heat transfer coefficients for air are;

$$\omega_{hv} = \left[\left(\left(\frac{1.37}{4 \left(\Delta T_c \right)^{0.75} l^{0.25}} \right) \omega_{\Delta T} \right)^2 + \left(- \frac{1.37 \left(\Delta T_c \right)^{0.25}}{4 l^{1.25}} \omega_l \right)^2 \right]^{\frac{1}{2}} \tag{A.12}$$

$$\omega_{hh,u} = \frac{2.49 \omega_{\Delta Tc}}{4 \Delta T_c^{0.75}} \tag{A.13}$$

$$\omega_{hh,d} = \frac{1.31 \omega_{\Delta Tc}}{4 \Delta T_c^{0.75}} \tag{A.14}$$

The uncertainty of the radiative heat transfer from both plates ω_{Qrad}, and that from each plate individually $\omega_{Qc,rad}$ and $\omega_{Qh,rad}$ are defined in Equations A.14 through A.16.

$$\omega_{Qrad} = \left[\omega_{Qc,rad}^2 + \omega_{h,rad}^2\right]^{\frac{1}{2}} \quad \text{(A.15)}$$

$$\omega_{Qh,rad} = \alpha_{Si}\sigma\left\{\left[\left(T_h^4 - T_{wall}^4\right)\omega_{Ah}\right]^2 + \left(4A_h T_h^3 \omega_{Th}\right)^2 + \left(4A_h T_{wall}^3 \omega_{Twall}\right)^2\right\}^{\frac{1}{2}} \quad \text{(A.16)}$$

$$\omega_{Qc,rad} = \alpha_{Si}\sigma\left\{\left[\left(T_c^4 - T_{wall}^4\right)\omega_{Ac}\right]^2 + \left(4A_c T_c^3 \omega_{Tc}\right)^2 + \left(4A_c T_{wall}^3 \omega_{Twall}\right)^2\right\}^{\frac{1}{2}} \quad \text{(A.17)}$$

The uncertainty of Q_{h-c} is:

$$\omega_{Qh-c} = \left[\omega_{Qout,cond}^2 + \omega_{c,conv}^2 + \omega_{c,rad}^2\right]^{\frac{1}{2}} \quad \text{(A.18)}$$

The uncertainty in total thermal contact resistance, ω_{Jth} is:

$$\omega_{Jth} = \begin{bmatrix} \left(\left(\dfrac{T_h - T_c}{Q_{h-c,cond}}\right)\omega_A\right)^2 + \left(\left(-A\dfrac{T_h - T_c}{Q_{h-c,cond}^2}\right)\omega_{Qh-c,cond}\right)^2 + \\ + \left(-\dfrac{\omega_{tSi}}{k_{Si}}\right)^2 + \left(-\dfrac{\omega_{tSiO2}}{k_{SiO2}}\right)^2 \end{bmatrix}^{\frac{1}{2}} \quad \text{(A.19)}$$

The uncertainty in area, ω_A, is calculated as;

$$\omega_A = \left[\left(w\omega_l\right)^2 + \left(l\omega_w\right)^2\right]^{\frac{1}{2}} \quad \text{(A.20)}$$

The thermal contact resistance, $J_{th,}$ is calculated as;

$$J_{th} = A\frac{T_h - T_c}{Q_{h-c}} - \frac{t_{Si}}{k_{Si}} - \frac{t_{SiO2}}{k_{SiO2}} \tag{A.21}$$

The uncertainty of $Q_{h-c,rad}$ as defined in Equation A.22 is;

$$Q_{h-c,rad} = Q_{h-c} - Q_{h-c,air} - Q_{h-c,wall} \tag{A.22}$$

$$\omega_{Qh-c,rad} = \left(\omega^2_{Q_{h-c}} + \omega^2_{Qh-c,air} + \omega^2_{Qh-c,wall}\right)^{\frac{1}{2}} \tag{A.23}$$

Table A.1 Uncertainty results

ωQH,Rad	ωQC,Rad	ωQrad	ω a b s	ωQabs	ωQh-c	ω J t h	J'th,si-sio2	ωJ'th, si-sio2	ωTh,surf	ωQh-c_cond_air	J'th,sio2-sio2	ωJ'th, sio2-sio2	ωQh-c_cond_wall	wQhc rad
0,041847	0,026914	0,049755	1,478081	111,6694	111,6695	0,027797	0,002915479	0,012354	2,344005	524,8364905	0,00072887	0,003088572	204,1311	574,10
0,041855	0,026914	0,049761	1,478081	112,5939	112,5939	0,027797	0,002915479	0,012354	2,347851	525,7009153	0,00072887	0,003088572	204,4928	575,20
0,041842	0,02691	0,049748	1,478081	112,4341	112,4341	0,027797	0,002915479	0,012354	2,347189	525,5511477	0,00072887	0,003088572	204,4095	575,00
0,041845	0,026912	0,049752	1,478081	112,1217	112,1217	0,027797	0,002915479	0,012354	2,345888	525,2585947	0,00072887	0,003088572	204,2881	574,63
0,041843	0,026909	0,049749	1,478081	112,4013	112,4013	0,027797	0,002915479	0,012354	2,34704	525,5182063	0,00072887	0,003088572	204,4059	574,97
0,041842	0,02691	0,049748	1,478081	112,2529	112,253	0,027797	0,002915479	0,012354	2,346436	525,3820403	0,00072887	0,003088572	204,3411	574,79
0,041846	0,026911	0,049752	1,478081	111,9733	111,9733	0,027797	0,002915479	0,012354	2,34527	525,1210773	0,00072887	0,003088572	204,2543	574,46
0,041848	0,026912	0,049754	1,478081	112,0332	112,0332	0,027797	0,002915479	0,012354	2,345507	525,1739141	0,00072887	0,003088572	204,27	574,53
0,041854	0,02691	0,049758	1,478081	112,805	112,8051	0,027797	0,002915479	0,012354	2,348712	525,8961542	0,00072887	0,003088572	204,6022	575,46
0,041852	0,026914	0,049759	1,478081	113,1175	113,1175	0,027797	0,002915479	0,012354	2,350035	526,1902439	0,00072887	0,003088572	204,668	575,81
0,041847	0,026911	0,049753	1,478081	113,0376	113,0376	0,027797	0,002915479	0,012354	2,349706	526,1165592	0,00072887	0,003088572	204,6397	575,72
0,041841	0,026909	0,049747	1,478081	112,9834	112,9834	0,027797	0,002915479	0,012354	2,349474	526,0635246	0,00072887	0,003088572	204,6035	575,65
0,041851	0.026909	0.049756	1.478081	111.9376	111.9377	0.027797	0.002915479	0.012354	2.345098	525.0849076	0.00072887	0.003088572	204.2839	574.44
0.041841	0.026913	0.049749	1.478081	112.7308	112.7309	0.027797	0.002915479	0.012354	2.34843	525.8279224	0.00072887	0.003088572	204.4888	575.34
0.04185	0.026913	0.049757	1.478081	111.7236	111.7237	0.027797	0.002915479	0.012354	2.344228	524.8873916	0.00072887	0.003088572	204.1667	574.17
0.041844	0.026912	0.049752	1.478081	111.8934	111.8934	0.027797	0.002915479	0.012354	2.344929	525.0434285	0.00072887	0.003088572	204.2052	574.36
0.041848	0.026913	0.049755	1.478081	112.3927	112.3928	0.027797	0.002915479	0.012354	2.347001	525.5091749	0.00072887	0.003088572	204.3967	574.95
0.041852	0.026915	0.04976	1.478081	112.2073	112.2073	0.027797	0.002915479	0.012354	2.346234	525.337318	0.00072887	0.003088572	204.3363	574.74
0.041846	0.026913	0.049753	1.478081	112.7437	112.7437	0.027797	0.002915479	0.012354	2.348475	525.8393272	0.00072887	0.003088572	204.5139	575.36
0.041847	0.026912	0.049754	1.478081	113.0704	113.0704	0.027797	0.002915479	0.012354	2.349833	526.1444236	0.00072887	0.003088572	204.6413	575.75
0.041844	0.026908	0.049749	1.478081	112.6381	112.6381	0.027797	0.002915479	0.012354	2.348018	525.7382603	0.00072887	0.003088572	204.5047	575.25
0.041846	0.026909	0.049752	1.478081	113.1774	113.1774	0.027797	0.002915479	0.012354	2.350282	526.2463225	0.00072887	0.003088572	204.699	575.89
0.041851	0.026912	0.049757	1.478081	112.2815	112.2815	0.027797	0.002915479	0.012354	2.34654	525.4068529	0.00072887	0.003088572	204.3797	574.83
0.04185	0.02691	0.049755	1.478081	112.8264	112.8265	0.027797	0.002915479	0.012354	2.348808	525.9165253	0.00072887	0.003088572	204.5893	575.48
0.041847	0.026912	0.049754	1.478081	112.8621	112.8621	0.027797	0.002915479	0.012354	2.348975	525.9519459	0.00072887	0.003088572	204.5672	575.51
0.041849	0.026911	0.049755	1.478081	112.3656	112.3657	0.027797	0.002915479	0.012354	2.346896	525.4865989	0.00072887	0.003088572	204.4067	574.93

ωQH,Rad	ωQC,Rad	ωQrad	ω a b s	ωQabs	ωQh-c	ω J t h	J'th,si-sio2	ωJ'th, si-sio2	ωTh,surf	ωQh-c_cond_air	J'th,sio2-sio2	ωJ'th, sio2-sio2	ωQh-c_cond_wall	wQhc rad
0.041843	0.026911	0.04975	1.478081	112.651	112.651	0.027797	0.002915479	0.012354	2.348082	525.751327	0.00072887	0.003088572	204.4833	575.25
0.041841	0.02691	0.049748	1.478081	111.5325	111.5325	0.027797	0.002915479	0.012354	2.343439	524.709078	0.00072887	0.003088572	204.0754	573.94
0.041845	0.026913	0.049752	1.478081	111.3227	111.3228	0.027797	0.002915479	0.012354	2.342572	524.5145378	0.00072887	0.003088572	203.9983	573.69
0.041846	0.026912	0.049753	1.478081	112.0318	112.0318	0.027797	0.002915479	0.012354	2.345513	525.1749658	0.00072887	0.003088572	204.2625	574.53
0.041849	0.026912	0.049756	1.478081	112.1802	112.1802	0.027797	0.002915479	0.012354	2.346115	525.3111017	0.00072887	0.003088572	204.3356	574.71
0.041849	0.026907	0.049752	1.478081	111.4454	111.4455	0.027797	0.002915479	0.012354	2.343053	524.6260671	0.00072887	0.003088572	204.1076	573.86
0.041846	0.026909	0.049751	1.478081	113.059	113.059	0.027797	0.002915479	0.012354	2.349777	526.1330196	0.00072887	0.003088572	204.6554	575.74
0.041841	0.026911	0.049748	1.478081	112.9876	112.9877	0.027797	0.002915479	0.012354	2.349497	526.0679744	0.00072887	0.003088572	204.5904	575.65
0.041851	0.026909	0.049756	1.478081	112.7095	112.7095	0.027797	0.002915479	0.012354	2.348321	525.8078624	0.00072887	0.003088572	204.559	575.34
0.041851	0.026908	0.049755	1.478081	113.5583	113.5583	0.027797	0.002915479	0.012354	2.351877	526.606311	0.00072887	0.003088572	204.8751	576.35
0.041845	0.026911	0.049752	1.478081	112.6952	112.6952	0.027797	0.002915479	0.012354	2.348271	525.7943045	0.00072887	0.003088572	204.5099	575.31
0.041847	0.02691	0.049753	1.478081	112.5839	112.5839	0.027797	0.002915479	0.012354	2.347808	525.6911719	0.00072887	0.003088572	204.4866	575.19
0.041846	0.026909	0.049751	1.478081	112.2772	112.2772	0.027797	0.002915479	0.012354	2.346526	525.4036068	0.00072887	0.003088572	204.376	574.83
0.041851	0.026909	0.049755	1.478081	112.4584	112.4584	0.027797	0.002915479	0.012354	2.347281	525.5747295	0.00072887	0.003088572	204.4721	575.05
0.041847	0.026912	0.049753	1.478081	112.4184	112.4184	0.027797	0.002915479	0.012354	2.347114	525.5345623	0.00072887	0.003088572	204.4088	574.98
0.04185	0.026912	0.049756	1.478081	112.4983	112.4983	0.027797	0.002915479	0.012354	2.347456	525.6123673	0.00072887	0.003088572	204.4587	575.09
0.041849	0.026913	0.049756	1.478081	112.3756	112.3756	0.027797	0.002915479	0.012354	2.346945	525.497095	0.00072887	0.003088572	204.4013	574.94
0.041842	0.026906	0.049747	1.478081	112.4469	112.447	0.027797	0.002915479	0.012354	2.347222	525.5598889	0.00072887	0.003088572	204.4385	575.02
0.041847	0.026908	0.049751	1.478081	112.8136	112.8136	0.027797	0.002915479	0.012354	2.348753	525.9040381	0.00072887	0.003088572	204.5845	575.46
0.041851	0.02691	0.049756	1.478081	112.6381	112.6381	0.027797	0.002915479	0.012354	2.348035	525.7435225	0.00072887	0.003088572	204.5304	575.26
0.04185	0.02691	0.049756	1.478081	112.066	112.0661	0.027797	0.002915479	0.012354	2.345642	525.2059085	0.00072887	0.003088572	204.3123	574.58
0.041848	0.026914	0.049756	1.478081	110.7578	110.7578	0.027797	0.002915479	0.012354	2.340245	523.9928871	0.00072887	0.003088572	203.8097	573.04
0.041853	0.026913	0.049759	1.478081	111.3285	111.3285	0.027797	0.002915479	0.012354	2.342598	524.5227742	0.00072887	0.003088572	204.0459	573.72
0.041847	0.026913	0.049754	1.478081	110.7264	110.7264	0.027797	0.002915479	0.012354	2.340123	523.9655434	0.00072887	0.003088572	203.7981	573.00
0.041845	0.026907	0.04975	1.478081	111.0859	111.086	0.027797	0.002915479	0.012354	2.34159	524.296794	0.00072887	0.003088572	203.9628	573.44
0.041849	0.026908	0.049753	1.478081	111.5282	111.5282	0.027797	0.002915479	0.012354	2.343418	524.7075832	0.00072887	0.003088572	204.1349	573.96
0.041851	0.026914	0.049759	1.478081	111.7094	111.7094	0.027797	0.002915479	0.012354	2.344172	524.8748079	0.00072887	0.003088572	204.1618	574.16
0.041856	0.026917	0.049764	1.478081	111.6751	111.6752	0.027797	0.002915479	0.012354	2.34403	524.8430582	0.00072887	0.003088572	204.152	574.12

ωQH,Rad	ωQC,Rad	ωQrad	ω a b s	ωQabs	ωQh-c	ω J t h	J'th,si-sio2	ωJ'th, si-sio2	ωTh,surf	ωQh-c_cond_air	J'th,sio2-sio2	ωJ'th, sio2-sio2	ωQh-c_cond_wall	wQhc rad
0.041854	0.026914	0.049761	1.478081	112.6538	112.6538	0.027797	0.002915479	0.012354	2.348117	525.7608758	0.00072887	0.003088572	204.5195	575.28
0.04185	0.026915	0.049758	1.478081	112.4983	112.4983	0.027797	0.002915479	0.012354	2.347464	525.6128501	0.00072887	0.003088572	204.4355	575.08
0.041855	0.026917	0.049763	1.478081	111.6908	111.6909	0.027797	0.002915479	0.012354	2.344109	524.8606852	0.00072887	0.003088572	204.1564	574.14
0.041857	0.026915	0.049764	1.478081	112.9891	112.9891	0.027797	0.002915479	0.012354	2.349509	526.0734474	0.00072887	0.003088572	204.6459	575.67
0.041852	0.026913	0.049758	1.478081	113.0333	113.0333	0.027797	0.002915479	0.012354	2.349705	526.1170801	0.00072887	0.003088572	204.6553	575.73
0.041852	0.026914	0.049759	1.478081	111.2443	111.2443	0.027797	0.002915479	0.012354	2.342254	524.4446502	0.00072887	0.003088572	203.9999	573.61

Appendix B: Measurement Results

Table B.1 Measurement results

T_h(°C)	T_c(°C)	Q_{meas}(mW)	Q _cond_air	Q_cond_wall	Q_{h-c}
24.051	23.486	7.83	34.85505025	12.29916462	41.43
24.07	23.48	7.89	38.36152874	13.53648191	41.77
24.034	23.466	7.88	34.95427634	12.33417814	41.71
24.04	23.48	7.86	33.84049142	11.94116123	41.60
24.051	23.475	7.88	36.24010549	12.78790362	41.70
24.031	23.466	7.87	34.56749798	12.19769718	41.65
24.043	23.466	7.85	36.60587916	12.91697274	41.54
24.062	23.489	7.85	35.94570516	12.68401973	41.56
24.092	23.475	7.91	42.53875814	15.01048444	41.85
24.07	23.491	7.93	36.36382699	12.83156074	41.97
24.051	23.472	7.92	36.4016411	12.84490406	41.94
24.045	23.48	7.92	34.21207463	12.07228034	41.92
24.084	23.472	7.85	42.17194814	14.88104963	41.52
24.031	23.489	7.90	30.69048029	10.82962919	41.82
24.059	23.48	7.83	37.04624866	13.0723642	41.45
24.051	23.491	7.84	33.954625	11.9814351	41.51
24.065	23.494	7.88	35.45308126	12.51018948	41.70
24.07	23.494	7.87	36.3347827	12.821312	41.63
24.051	23.489	7.90	33.85356577	11.94577473	41.83
24.065	23.494	7.93	35.12088788	12.3929697	41.95
24.065	23.477	7.90	38.02692774	13.41841257	41.79
24.062	23.475	7.93	37.60226564	13.26856372	41.99
24.07	23.48	7.87	38.51643746	13.59114394	41.65
24.076	23.475	7.91	39.99275193	14.11208522	41.86
24.048	23.477	7.91	35.21997623	12.42793462	41.87
24.059	23.472	7.88	37.99878873	13.40848327	41.69
24.051	23.486	7.90	34.37541015	12.12991591	41.79
24.034	23.475	7.82	33.97159303	11.98742254	41.38
24.04	23.483	7.80	33.75728447	11.91180033	41.30
24.043	23.477	7.85	34.83496999	12.29207898	41.56
24.07	23.486	7.86	37.61651876	13.27359317	41.62
24.081	23.469	7.81	42.41409832	14.96649621	41.34

Th(°C)	Tc(°C)	Qmeas(mW)	Q _cond_air	Q_cond_wall	Qh-c
24.07	23.483	7.92	37.66224859	13.28972967	41.94
24.037	23.486	7.92	31.99140777	11.28868235	41.92
24.076	23.466	7.90	41.47516151	14.63517727	41.81
24.078	23.461	7.96	42.16774832	14.87956766	42.13
24.051	23.477	7.90	35.77821628	12.62491859	41.81
24.054	23.466	7.89	38.04991417	13.4265237	41.77
24.054	23.466	7.87	38.20090711	13.47980399	41.65
24.065	23.453	7.88	41.91321682	14.78975212	41.72
24.056	23.483	7.88	35.75604417	12.61709481	41.71
24.054	23.464	7.89	38.40747202	13.55269373	41.74
24.051	23.472	7.88	36.72519115	12.95907389	41.69
24.059	23.469	7.88	38.43696281	13.56310003	41.71
24.07	23.469	7.91	39.99947822	14.11445871	41.85
24.062	23.455	7.90	41.0323409	14.4789209	41.79
24.07	23.472	7.86	39.88944374	14.07563127	41.57
24.043	23.475	7.76	35.77554179	12.62397486	41.09
24.056	23.461	7.80	39.77253043	14.03437653	41.30
24.031	23.464	7.76	35.63083531	12.57291285	41.08
24.045	23.447	7.79	40.36786038	14.24444827	41.21
24.056	23.447	7.82	41.89362463	14.78283871	41.38
24.059	23.48	7.83	37.05256074	13.07459152	41.44
24.07	23.489	7.83	37.386128	13.19229608	41.43
24.051	23.458	7.90	38.8037555	13.69252873	41.80
24.045	23.475	7.89	35.23809107	12.43432673	41.74
24.051	23.472	7.83	37.05856567	13.07671045	41.44
24.07	23.472	7.92	39.43351956	13.9147511	41.92
24.045	23.453	7.92	38.45911211	13.57091577	41.94
24.051	23.469	7.80	37.75398457	13.32210019	41.27